

Hydrodynamical Simulations of Circumbinary Accretion: Balance between Heating and Cooling

Hai-Yang Wang,¹★ Xue-Ning Bai,²† Dong Lai³‡ Douglas N. C. Lin^{2,4}§

¹*Fudan University, Department of Physics, Shanghai 200433, China*

²*Institute for Advanced Study and Department of Astronomy, Tsinghua University, Beijing 100084, China*

³*Department of Astronomy, Center for Astrophysics and Planetary Science, Cornell University, Ithaca, NY 14853, USA*

⁴*Department of Astronomy & Astrophysics, University of California, Santa Cruz, CA 95064, USA*

Accepted XXX. Received YYY; in original form ZZZ

ABSTRACT

Hydrodynamical interaction in circumbinary discs (CBDs) plays a crucial role in various astrophysical systems, ranging from young stellar binaries to supermassive black hole binaries in galactic centers. Most previous simulations of binary-disc systems have adopted locally isothermal equation of state. In this study, we use the grid-based code *Athena++* to conduct a suite of two-dimensional viscous hydrodynamical simulations of circumbinary accretion on a cartesian grid, resolving the central cavity of the binary. The gas thermodynamics is treated by thermal relaxation towards an equilibrium temperature (based on the constant- β cooling ansatz, where β is the cooling time in units of the local Keplerian time). Focusing on equal mass, circular binaries in CBDs with (equilibrium) disc aspect ratio $H/R = 0.1$, we find that the cooling of the disc gas significantly influences the binary orbital evolution, accretion variability, and CBD morphology, and the effect depends sensitively on the disc viscosity prescriptions. When adopting a constant kinematic viscosity, a finite cooling time ($\beta \gtrsim 0.1$) leads to binary inspiral as opposed to outspiral and the CBD cavity becomes more symmetric. When adopting a dynamically varying α -viscosity, binary inspiral only occurs within a narrow range of cooling time (corresponding to β around 0.5).

Key words: accretion, accretion discs - binaries: general - hydrodynamics - methods: numerical

1 INTRODUCTION

Circumbinary discs (CBDs) can be present around a wide range of binary systems, and play a crucial role in their evolution. In the star formation context, CBDs can form as a natural product of disc or core fragmentations and dynamical interactions (Boss 1986; Bonnell & Bate 1994a,b; Kratter et al. 2008). While the CBDs affect binary evolution, binaries can also leave observable imprints on the CBDs; examples include Class I/II systems GG Tau, DQ Tau and UZ Tau E (Dutrey et al. 1994; Bertin & Arnouts 1996; Mathieu et al. 1997) and Class 0 system L1448 IRS3B (Tobin et al. 2016). Moreover, the discovery of circumbinary planets (e.g., Hamers et al. 2018 and references therein) triggered substantial interest in studying planet formation and migration in CBDs, which are closely connected to binary-disc interactions (Kley & Haghighipour 2014, 2015; Mutter et al. 2017; Thun & Kley 2018; Penzlin et al. 2021).

CBDs are also expected to form around binary supermassive black holes (SMBHs) following galaxy mergers. They may play a key role in the orbital evolution of SMBH binaries, especially for orbital separations between ~ 0.01 and ~ 1 pc. At larger separations, dynamical friction by gas and star and stellar “loss-cone” scattering are effective

in driving the orbital decay of binary SMBHs ($\gtrsim 1$ pc, e.g., Escala et al. 2005), while at small separations the emission of gravitational waves is effective ($\lesssim 0.01$ pc, e.g., Jaffe & Backer 2003; Wyithe & Loeb 2003; Sesana et al. 2008; Kelley et al. 2017). The orbital evolution of SMBH binaries in the intermediate range, known as the “final parsec problem”, has been a central topic of theoretical studies of CBDs (Begelman et al. 1980; Armitage & Natarajan 2002; MacFadyen & Milosavljević 2008; Haiman et al. 2009).

Without accretion, a binary is expected to lose angular momentum to its CBD through resonantly excited trailing density waves (Goldreich & Tremaine 1979). Some earlier numerical simulations have claimed a negative torque exerted on the binary (e.g., MacFadyen & Milosavljević 2008), but this likely reflects the “transient” state of the simulation, as the flow has not reached a quasi-steady state. In general, the CBD is not only the source of torque acting on the binary. The accretion streams penetrating the disc cavity and the mini-discs formed around each binary component can also provide non-negligible amount of gravitational torque, as well as the torque stems from direct accretion onto the binary. All these torque components must be included and time-averaged in simulations of sufficiently long durations in order to determine the long-term orbital evolution of the binary.

Recently, significant progress has been made towards more comprehensive understandings of CBD physics through numerical simulations, most of which are conducted in 2D viscous hydrodynamics (see Lai & Muñoz 2022 for a review). It has been recognized that

★ cgmgalaxy0721@gmail.com

† xbai@tsinghua.edu.cn

‡ dong@astro.cornell.edu

§ lin@ucolick.org

reaching a quasi-steady state of the flow is needed before applying diagnostics to calculate binary orbital evolution (e.g., [Miranda et al. 2017; Muñoz et al. 2019, 2020](#)). As the most extensively studied case, equal-mass, circular binaries in CBDs with disc aspect ratio $h = H/r = 0.1$ were found to experience orbital expansion (e.g., [Miranda et al. 2017; Muñoz et al. 2019](#)). This result has been confirmed by other in the 2D and 3D simulations ([Moody et al. 2019](#)), and is largely insensitive to the choices of sink prescriptions ([Dittmann & Ryan 2021](#)) and boundary conditions ([Muñoz et al. 2020](#)) for the binary components. Later, it was found that the dynamics of the CBDs and the torque exerted on the binary can sensitively depend on parameters related to the binary and disc properties: Binary will experience a transition from outspiral to inspiral when the disc aspect ratio $h \lesssim 0.04$, ([Heath & Nixon 2020; Tiede et al. 2020; Dittmann & Ryan 2022](#)), or when the mass ratio $q \lesssim 0.05$ ([Muñoz et al. 2020; Duffell et al. 2020](#)). The orbit of the binary can also expand or shrink depending on the eccentricity of the binary ([Muñoz & Lai 2016; Muñoz et al. 2019, 2020; D’Orazio & Duffell 2021; Zrake et al. 2021](#)) and the viscosity in the CBD ([Duffell et al. 2020; Penzlin et al. 2022; Dittmann & Ryan 2022](#)).

All the studies mentioned above have adopted the locally isothermal equation of state, i.e., assuming the disc temperature is a fixed function of position such that the disc aspect ratio h is a constant. There are only a handful of works that consider different gas thermodynamics. Most of these focused on other aspects of the problem, such as the role of self-gravity ([Franchini et al. 2021](#)), the evolution of disc cavity and modeling of specific binary systems ([Thun & Kley 2018; Kley et al. 2019; Sudarshan et al. 2022](#)). Cooling in the CBDs is also included in some GRMHD simulations, in the regime near binary merger (e.g., [Noble et al. 2012; d’Ascoli et al. 2018; Noble et al. 2021](#)).

In our previous work ([Wang et al. 2022c](#)), we studied the effect of dynamical cooling (use the β prescription; see below) on disc morphology, binary accretion variability and binary orbital evolution using cylindrical-grid simulations with excised binary cavity. We found that with a longer cooling time, the disc becomes more symmetric and the accretion variability is gradually suppressed. We also found that the relationship between the rate of angular momentum transport and the cooling time exhibits a “v”-shaped structure. Namely, the rate of angular momentum transport first decreases to a minimum value then increases as the cooling time increases. However, we can only explore a very limited parameter space using cylindrical-grid simulations with an excised central cavity – such simulations do not capture the mini-discs and accretion streams around individual binary components.

In this paper, we aim at a comprehensive study on how the gas thermodynamics affects binary-CBD interactions. Same as [Wang et al. \(2022c\)](#), we consider an equal mass binary on a fixed circular orbit, and treat the disc thermodynamics through dynamical cooling, relaxing disc temperature to a given temperature profile over a cooling time t_{cool} ([Gammie 2001](#)). A significant improvement is that we resolve the mini-discs around each binary component by carrying out simulations in the cartesian geometry. In doing so, we find that in addition to the cooling time, different temperature and viscosity prescriptions in the central cavity and the mini-discs also have a significant impact on the CBD-binary system.

This paper is organized as follows. In Section 2, we describe our simulation setup and diagnostics. In Section 3, we present the simulation results, especially on the impact of different cooling/heating prescriptions on binary orbital evolution, accretion variability and disc morphology. We also briefly discuss a more comprehensive pa-

rameter survey of different temperature and viscosity profiles. Finally, we conclude in Section 4.

2 PROBLEM SETUP

In this study, we use the grid-based Godunov code **ATHENA++** ([Stone et al. 2020](#)) to solve the vertically integrated viscous hydrodynamic equations in 2D cartesian coordinates (x, y) (similar to [Moody et al. 2019](#)). The continuity, momentum and energy equations in conservative form read

$$\frac{\partial \Sigma}{\partial t} + \nabla \cdot (\Sigma \mathbf{v}) = s_{\Sigma}, \quad (1)$$

$$\frac{\partial (\Sigma \mathbf{v})}{\partial t} + \nabla \cdot (\Sigma \mathbf{v} \mathbf{v} + P \mathbf{I}) = s_{\mathbf{p}} - \Sigma \nabla \Phi - \nabla \cdot \mathcal{T}_{\text{visc}}, \quad (2)$$

$$\frac{\partial E}{\partial t} + \nabla \cdot [(E + P) \mathbf{v}] = s_E - \Sigma \mathbf{v} \cdot \nabla \Phi + \Lambda - \nabla \cdot (\mathcal{T}_{\text{visc}} \mathbf{v}), \quad (3)$$

where Σ , \mathbf{v} are the disc surface density and velocity, P is the vertically integrated pressure, \mathbf{I} is the identity tensor, Φ is the gravitational potential, $\mathcal{T}_{\text{visc}}$ is the viscous stress tensor, E is the total energy density, Λ is the cooling term (to be specified in Section 2.2), and s_{Σ} , $s_{\mathbf{p}}$ and s_E are the sink terms for surface density, momentum and energy (to be specified in Section 2.4). The viscous stress tensor is given in the form of

$$\mathcal{T}_{\text{visc},ij} = -\Sigma \nu \left(\frac{\partial v_i}{\partial x_j} + \frac{\partial v_j}{\partial x_i} - \frac{2}{3} \frac{\partial v_k}{\partial x_k} \delta_{ij} \right), \quad (4)$$

with ν being the kinematic viscosity, which will be discussed in detail in Section 2.1. The total energy density is given by

$$E = \frac{1}{2} \Sigma v^2 + \frac{P}{\gamma - 1}, \quad (5)$$

where $\gamma = 5/3$ is the adiabatic index. Viscous heating is automatically included in the code, which enters the energy equation in the form of

$$Q_{\text{visc}} = -\nabla \cdot (\mathcal{T}_{\text{visc}} \mathbf{v}), \quad (6)$$

Same as [Wang et al. \(2022c\)](#), we assume equal-mass binary on a fixed circular orbit, with the mass of each component $M_1 = M_2 = 0.5 M_{\text{B}}$ and the binary separation a_{B} . Here we denote M_{B} as the total mass of the binary. The gravitational potential of the binary can be expressed as

$$\begin{aligned} \Phi(\mathbf{r}, t) &= \Phi_1 + \Phi_2 \\ &= - \sum_{i=1}^2 \frac{GM_i}{(|\mathbf{r} - \mathbf{r}_i|^2 + \epsilon^2)^{1/2}}, \end{aligned} \quad (7)$$

with the gravitational softening length $\epsilon = 0.025 a_{\text{B}}$, where \mathbf{r} specifies the location of gas element and \mathbf{r}_i the location of each binary component. The binary rotates counter-clockwise with Keplerian speed and the CBD evolves under this rotating potential.

Our coordinate system centers on the center-of-mass of the binary with computational domain covering $[-20a_{\text{B}}, 20a_{\text{B}}] \times [-20a_{\text{B}}, 20a_{\text{B}}]$ in x, y direction respectively. At the root level, the resolution is 256×256 . We take the advantage of adaptive mesh refinement (AMR) in **Athena++** and apply 4 more levels of refinement. In the domain covering the CBD cavity ($r \leq 2.5a_{\text{B}}$), the resolution is the highest, with $\Delta x = \Delta y = 0.0098 a_{\text{B}}$. We also ensure that at least one (two) more refinement level is applied within $[-10a_{\text{B}}, 10a_{\text{B}}] \times [-10a_{\text{B}}, 10a_{\text{B}}]$ ($[-5a_{\text{B}}, 5a_{\text{B}}] \times [-5a_{\text{B}}, 5a_{\text{B}}]$) comparing to the root grid. The accretion process is simulated through sink cells in the vicinity of the binary (see Section 2.4 for details).

We roughly resolve the sink cell with 10 grid cells along either the horizontal or vertical direction. At the boundary in both x and y directions, we use the outflow boundary condition. We also impose a damping zone between $[r_{\text{in}}, r_{\text{out}}] = [18a_B, 20a_B]$ (e.g., [Moody et al. 2019](#)) to quench modes characterized by azimuthal number $m = 4$, to suppress the impact of the square boundary, and to maintain the constant mass supply:

$$\frac{du}{dt} = -\frac{(r - r_{\text{in}})r}{(r_{\text{out}} - r_{\text{in}})r_{\text{out}}} \frac{(u - u_{\text{eq}})}{t_{\text{damp}}}, \quad (8)$$

with u representing hydrodynamic variables: (Σ, P, v_r, v_ϕ) , u_{eq} being the initial value of these variables, $t_{\text{damp}} = 10^{-3}/\Omega_B$ and $\Omega_B = \sqrt{GM_B/a_B^3}$ the orbital frequency of the binary.

2.1 “Equilibrium” Temperature Profile and Viscosity Prescription

Previous simulations of CBDs have adopted either locally or globally isothermal equation of state. In this work, we solve the energy equation of the flow and include gas cooling using a thermal relaxation ansatz (see Section 2.2). To this end, we need to specify the gas “equilibrium” temperature profile, which is the target of the thermal relaxation process.

2.1.1 “Equilibrium” Temperature Profile

We consider two types of “equilibrium” temperature profiles in this paper:

(i) Temp Type I (t1) :

$$T_{\text{eq}} \equiv c_s^2 = h^2 |\Phi|, \quad (9)$$

where c_s is the sound speed and Φ is given by Equation 7. Note that when close to one of the binary components, $|\mathbf{r} - \mathbf{r}_i| \ll |\mathbf{r} - \mathbf{r}_j|$, we have $T_{\text{eq}} \rightarrow h^2 GM_i/|\mathbf{r} - \mathbf{r}_i|$; and when far from the binary, $|\mathbf{r}| \gg |\mathbf{r}_1|, |\mathbf{r}_2|$, we have $T_{\text{eq}} \rightarrow h^2 GM_B/|\mathbf{r}|$.

(ii) Temp Type II (t2) :

$$T_{\text{eq}} \equiv c_s^2 = h^2 \Phi_{\text{eff}} = h^2 (|\Phi_B|^{-n} + |\Phi_K|^{-n})^{-1/n}, \quad (10)$$

where $\Phi_K = -GM_B/r$ and $\Phi_B = -GM_B/a_B$, which acts as a “softening” potential to avoid singularity in temperature profile; we adopt $n = 4$. Obviously, the two temperature profiles are the same for $r \gg a_B$, but can differ significantly for $r \lesssim a_B$.

2.1.2 Viscosity Prescription

In most CBD studies, viscosity adopted in the simulations is either constant or α -viscosity ([Shakura & Sunyaev 1973](#)). When adopting the α -viscosity, the viscosity profile $\nu = \alpha c_s H$ (H is the disc scale height) can be centered around each of the binary component or the coordinate center, similar to the two different temperature profile types. But in some cases, employing such an α -viscosity in the simulation can be problematic: The viscous time in the disc scale grows quadratically with the Mach number v_K/c_s , making it computationally challenging for thin discs ($h \lesssim 0.05$) to reach a quasi-steady state. Consequently, constant kinematic viscosity coefficients are adopted by some studies (e.g., [Tiede et al. 2020](#); [Duffell et al. 2020](#); [Dittmann & Ryan 2021, 2022](#)). In this paper, we adopt

two viscosity prescriptions mentioned above. In order to straightforwardly compare simulations adopting different viscosity profiles, all of the simulations in this study use $\alpha = 0.1$ and $h = 0.1$.

(i) Visc Type I (n1) : When adopting constant kinematic viscosity, we choose

$$\nu = \alpha h^2 a_B^2 \Omega_B, \quad (11)$$

with $\alpha = 0.1$ and $h = 0.1$, which gives $\nu = 10^{-3} a_B^2 \Omega_B$.

(ii) Visc Type II (n2) : When adopting α -viscosity, we can have two different types. The viscosity profile depends on the temperature profile chosen in the simulation. In the simulations employing an axisymmetric equilibrium temperature profile (see Equation 10), the viscosity profile is also axisymmetric

$$\begin{aligned} \nu &= \alpha c_s H = \alpha \frac{T}{\Omega_{\text{eff1}}} \\ &= \alpha \frac{T}{(|\Omega_B|^{-n} + |\Omega_K|^{-n})^{-1/n}}, \end{aligned} \quad (12)$$

where we choose $n = 2$.

(iii) Visc Type III (n3) : In the simulations employing the temperature profile which centers around each of the binary component, the viscosity profile is

$$\begin{aligned} \nu &= \alpha c_s H = \alpha \frac{T}{\Omega_{\text{eff2}}} \\ &= \alpha \frac{T}{(|\Omega_1|^{-n} + |\Omega_2|^{-n})^{-1/n}}, \end{aligned} \quad (13)$$

where $n = 2$, $\Omega_1 = \sqrt{GM_1/(|\mathbf{r} - \mathbf{r}_1|^2 + \epsilon^2)^{3/2}}$, and $\Omega_2 = \sqrt{GM_2/(|\mathbf{r} - \mathbf{r}_2|^2 + \epsilon^2)^{3/2}}$. Here we choose $n = 2$ so that the viscosity profile is similar to the one widely used in previous studies $\nu = \alpha T/\Omega_{\text{eff}}$ (e.g., [Muñoz & Lai 2016](#); [Muñoz et al. 2019](#)). Same as [Muñoz et al. \(2019\)](#), Ω_{eff} reduces to $\sqrt{GM_B/|\mathbf{r}|}$ far from the binary and to $\sqrt{GM_i/|\mathbf{r} - \mathbf{r}_i|}$ close to one of the binary components. Consequently, the viscosity reduces to

$$\nu \rightarrow \alpha \frac{T}{\Omega_K} = \alpha \frac{GM_B/|\mathbf{r}|}{\sqrt{GM_B/|\mathbf{r}|^3}}, \quad (14)$$

when $|\mathbf{r}| \gg |\mathbf{r}_1|, |\mathbf{r}_2|$, which is equivalent to the α -viscosity in accretion discs hosting single binary component. And when $|\mathbf{r} - \mathbf{r}_i| \ll |\mathbf{r} - \mathbf{r}_j|$, the viscosity reduces to

$$\nu \rightarrow \alpha \frac{T}{\Omega_i} = \alpha \frac{GM_i/|\mathbf{r} - \mathbf{r}_i|}{\sqrt{GM_i/|\mathbf{r} - \mathbf{r}_i|^3}}, \quad (15)$$

In this way, the viscosity in each of the mini-disc can also be regarded as standard α -viscosity. The 2D/1D temperature and viscosity profiles are separately illustrated in the upper/lower panels of Figure 1.

2.2 Thermal Relaxation

As in [Wang et al. \(2022c\)](#), we thermally relax gas temperature to the prescribed “equilibrium” value of T_{eq} over a cooling timescale t_{cool} , controlled by the cooling term

$$\Lambda = -\frac{\Sigma}{\gamma - 1} \times \frac{(T - T_{\text{eq}})}{t_{\text{cool}}}, \quad (16)$$

We prescribe the cooling time in a scale-free manner, using the dimensionless parameter

$$\beta \equiv \Omega_{\text{eff2}} t_{\text{cool}}, \quad (17)$$

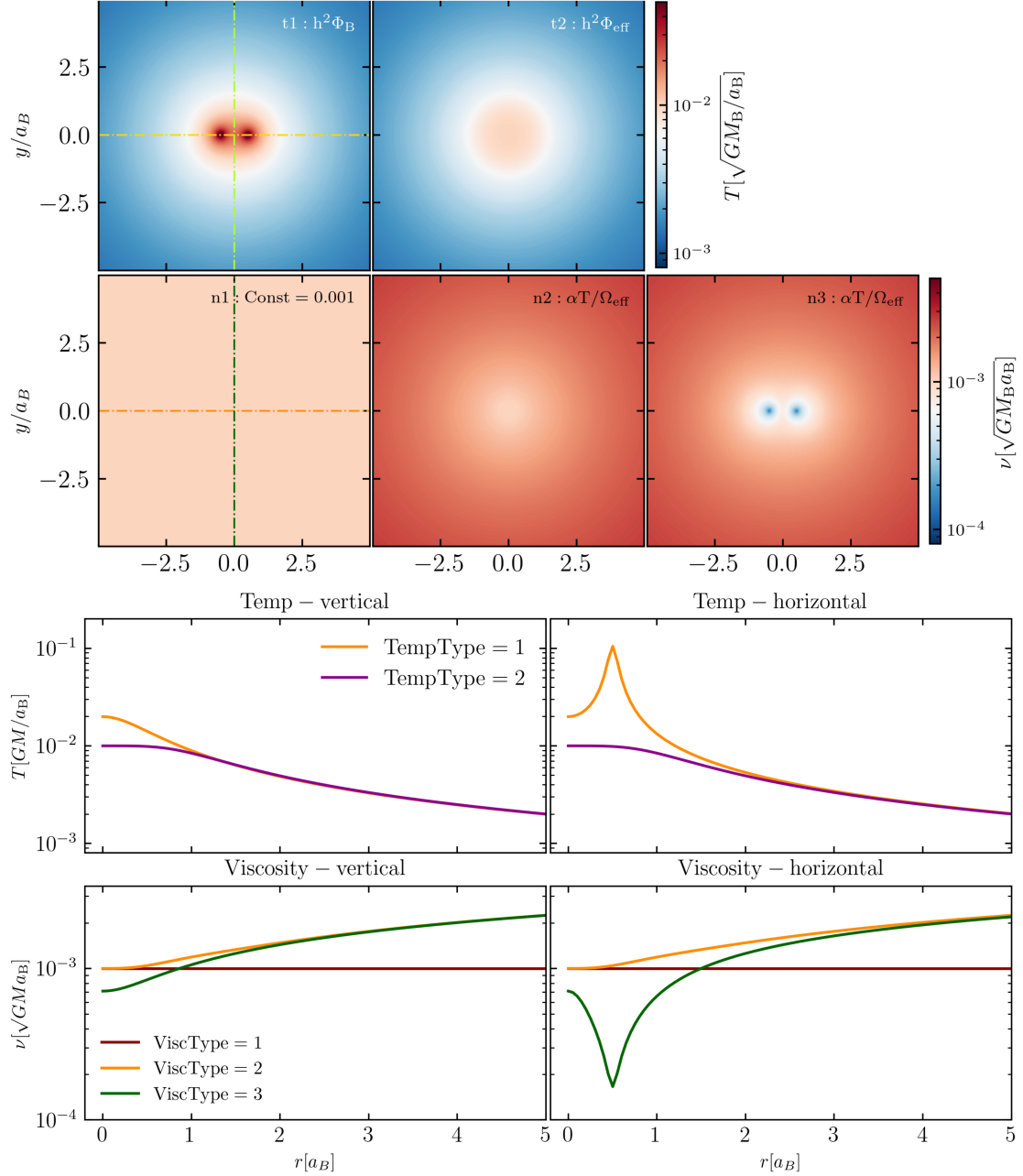


Figure 1. 2D and 1D illustrations of the “equilibrium” temperature profiles and the viscosity profiles employed in our simulations. The 2D temperature and viscosity distributions are shown in the upper panels. The first and the second rows in the lower panels show the 1D temperature and viscosity profiles along the green dash-dotted vertical and yellow dashed horizontal lines in the 2D plots.

known as dynamical cooling (or β -cooling) (Gammie 2001). Here the effective “orbital frequency” is given by (see Equation 13).

$$\Omega_{\text{eff}2} = (|\Omega_1|^{-n} + |\Omega_2|^{-n})^{-1/n} \quad (18)$$

The temperature of the CBD is expected to reach a new equilibrium T'_{eq} as a result of the combined effects of dynamical cooling and viscous heating. When assuming α -viscosity, the latter is $Q_{\text{visc}} \approx \frac{9}{4} \nu \Sigma \Omega_K^2$ (e.g., Frank et al. 1985). Neglecting the effect of compressional heating ($\nabla \cdot \mathbf{u} = 0$), we can expect a modified tem-

perature profile T'_{eq}

$$Q_{\text{visc}} + \Lambda = 0, \quad (19)$$

$$\Rightarrow T'_{\text{eq}} = \frac{T_{\text{eq}}}{1 - k\alpha\beta}; \quad k = \frac{9}{4}(\gamma - 1). \quad (20)$$

As the viscosity and cooling time increases, the new equilibrium temperature will increase accordingly.

To determine the range of cooling parameter β in our survey, we should refer to realistic scenarios, as the temperature distribution in CBDs is determined by the balance of radiative cooling and viscous heating. Following Equation 20 and requiring the denominator

to be non-zero, we find $\beta \lesssim 6$. In the following, we will conduct simulations with $\beta \in [0.0, 0.2, 0.5, 1.0, 2.0, 4.0]$.

2.3 Initial Condition

We use axisymmetric initial conditions with the outer CBD in an approximately viscous steady state. Focusing on fixed circular orbit, equal-mass binary with disc aspect ratio $h = 0.1$, the surface density profile in the initial setup is given by

$$\Sigma(r) = \Sigma_0(r) \exp \left[- \left(\frac{r}{r_{\text{edge}}} \right)^{-6} \right], \quad (21)$$

with $r_{\text{edge}} = 2.5a_B$ and $\Sigma_0(r) = \dot{M}_0/(3\pi\nu)$. The exponential cutoff factor creates an artificial cavity around the binary and r_{edge} is an initial guess of the cavity radial size. Here ν depends on our choice of viscosity prescription.

The initial radial velocity is set to be

$$v_r(r) = -\frac{3\nu}{2r} \exp \left[- \left(\frac{r}{r_{\text{edge}}} \right)^{-6} \right], \quad (22)$$

And we choose initial angular velocity to be

$$\Omega(r) = \left[\Omega_0(r)^{-4} + \Omega_B^{-4} \right]^{-1/4}, \quad (23)$$

where Ω_0 is the equilibrium angular velocity far from the binary

$$\Omega_0 = \sqrt{\frac{GM_B}{r^3}} (1 - h^2), \quad (24)$$

We apply an exponential cutoff in the initial radial velocity profile in Equation 22 and a “softened” initial azimuthal velocity profile in Equation 24 inside the CBD cavity to avoid violent relaxation at the beginning of the simulation. Our simulations are scale-free, with $G = M_B = a_B = \Omega_B = 1$ in code units, thus the binary period is $P_B = 2\pi$. As we have stated in Section 2.1, viscosity is parameterized by choosing $\alpha = 0.1$ and $h = 0.1$. And the mass injection rate is given as $\dot{M}_0 = 3\pi\alpha h^2$.

2.4 The Sink Term

As the accretion of each binary component is simulated through the sink cells, we remove the mass, angular momentum, and energy according to the torque-free scheme (similar to, e.g., [Dempsey et al. 2020](#); [Dittmann & Ryan 2022](#)). The sink terms for surface density s_Σ , momentum s_p , and energy s_E are given as follows:

$$\begin{aligned} s_\Sigma &= s_{\Sigma,1} + s_{\Sigma,2} \\ &= -\frac{\Sigma}{t_s} \left[\exp \left(- \left(\frac{|\mathbf{r} - \mathbf{r}_1|}{r_s} \right)^4 \right) + \exp \left(- \left(\frac{|\mathbf{r} - \mathbf{r}_2|}{r_s} \right)^4 \right) \right], \end{aligned} \quad (25)$$

$$\begin{aligned} s_p &= s_{p,1} + s_{p,2} \\ &= -\frac{\Sigma}{t_s} \left[\exp \left(- \left(\frac{|\mathbf{r} - \mathbf{r}_1|}{r_s} \right)^4 \right) \mathbf{v}_1^{\text{res}} + \exp \left(- \left(\frac{|\mathbf{r} - \mathbf{r}_2|}{r_s} \right)^4 \right) \mathbf{v}_2^{\text{res}} \right], \end{aligned} \quad (26)$$

$$\begin{aligned} s_E &= s_{E,1} + s_{E,2} \\ &= -\frac{\Sigma}{t_s} \left[\exp \left(- \left(\frac{|\mathbf{r} - \mathbf{r}_1|}{r_s} \right)^4 \right) E_1^{\text{res}} + \exp \left(- \left(\frac{|\mathbf{r} - \mathbf{r}_2|}{r_s} \right)^4 \right) E_2^{\text{res}} \right], \end{aligned} \quad (27)$$

$$\mathbf{v}_i^{\text{res}} = (\mathbf{v} - \mathbf{v}_i) \cdot \hat{r}_i \hat{r}_i + \mathbf{v}_i, \quad (28)$$

$$E_i^{\text{res}} = \frac{1}{2} \mathbf{v}_i^{\text{res}} \cdot \mathbf{v}_i^{\text{res}} + \frac{T}{\gamma - 1}, \quad (29)$$

where $s_{\Sigma,i}$, $s_{p,i}$, and $s_{E,i}$ are separately the sink terms for surface density, momentum and energy of each binary component, $r_s = 0.05a_B$ is the radius of the sink cell, t_s is the sink timescale; $\mathbf{v}_i^{\text{res}}$ is the “extracted” velocity of the sink cell in comoving frame of the binary, \mathbf{v}_i is the velocity of the i th binary component, E_i^{res} is the “extracted” specific energy of the sink cell, and \hat{r}_i is the unit basis vectors in the polar coordinate centered on each binary component in radial direction.

In the comoving frame of the sink cell, only momentum in the radial direction is absorbed. The major difference between the standard sink term and torque-free sink term is that the latter does not extract angular momentum associated with the mass accreted in the sink radius. For most of the simulations, we choose sink time $t_s = (\gamma_s \Omega_B)^{-1}$ with $\gamma_s = 3.0$. The only exception is that in the simulations adopting dynamically varying α -viscosity and axisymmetric temperature profile (namely, runs t2n2b- in Table 1), we instead choose the sink time to be

$$t_s = \frac{2|\mathbf{r} - \mathbf{r}_i|^2}{3\nu}. \quad (30)$$

Choosing this t_s would avoid mass accumulation, and the final results are barely affected by this different sink prescription as we will show in Section 3.3.

2.5 Diagnostics

All of the simulations are run for 2200 binary orbits. After reaching a quasi-steady state, the net rate of angular momentum transfer across the CBD should be the same as the angular momentum transfer rate between CBD and the binary. In this work, we separately calculate these transfer rates. First, the total torque \dot{J}_{tot} on the binary can be computed as the sum of accretion torque \dot{J}_{acc} and gravitational torque \dot{J}_{grav} , given by

$$\dot{J}_{\text{tot}} = \dot{J}_{\text{acc}} + \dot{J}_{\text{grav}}, \quad (31)$$

$$\dot{J}_{\text{acc},i}|_{i=1,2} = \hat{\mathbf{e}}_z \cdot \int \mathbf{r} \times s_{p,i} dA, \quad (32)$$

$$\dot{J}_{\text{grav},i}|_{i=1,2} = -\hat{\mathbf{e}}_z \cdot \int \mathbf{r} \times (\Sigma \nabla \Phi_i) dA, \quad (33)$$

Because binary orbital evolution is determined by the specific torque ($\dot{J}_{\text{tot}}/\dot{M}$, where $\dot{M} = \dot{M}_1 + \dot{M}_2$), we also store the accretion rate of each sink cell

$$\dot{M}_i|_{i=1,2} = - \int s_{\Sigma,i} dA, \quad (34)$$

These values are outputted as time series every 1/100 binary orbit. We use the time-averaged specific torque in the last 200 orbits to determine the orbital evolution of the binary.

The second method is to calculate the angular momentum flux in the CBD. Same as [Wang et al. \(2022c\)](#), the advective, viscous, gravitational and total torques along with the accretion rate are given

by (e.g., [Miranda et al. 2017](#); [Muñoz et al. 2019](#); [Moody et al. 2019](#)):

$$\begin{aligned} j_{\text{adv}} &= \hat{e}_z \cdot \oint \Sigma \mathbf{v} \times \mathbf{r} (\mathbf{v} \cdot \mathbf{r}) d\phi \\ &= - \oint r^2 \Sigma v_r v_\phi d\phi, \end{aligned} \quad (35)$$

$$\begin{aligned} j_{\text{visc}} &= -\hat{e}_z \cdot \oint (\mathcal{T}_{\text{visc}} \cdot \mathbf{r}) \times \mathbf{r} d\phi, \\ &= - \oint r^3 \nu \Sigma \left[\frac{\partial}{\partial r} \left(\frac{v_\phi}{r} \right) + \frac{1}{r^2} \frac{\partial v_r}{\partial \phi} \right] d\phi, \end{aligned} \quad (36)$$

$$\begin{aligned} T_{\text{grav}} &= \hat{e}_z \cdot \int_r^{r_{\text{out}}} \left[- \oint \Sigma (\mathbf{r} \times \nabla \Phi) d\phi \right] dr \\ &= \int_r^{r_{\text{out}}} \left(- \oint r \Sigma \frac{\partial \Phi}{\partial \phi} d\phi \right) dr, \end{aligned} \quad (37)$$

$$j_{\text{tot}} = j_{\text{adv}} - j_{\text{visc}} - T_{\text{grav}}, \quad (38)$$

$$\dot{M} = - \oint \Sigma v_r r d\phi, \quad (39)$$

These radial profiles of angular momentum flux are calculated in each timestep, and time-averaged results are generated by post-processing the outputted, time-integrated values. Same as the first method, we use time-averaged results from the last 200 binary orbits when the inner disc has reached a quasi-steady state.

For equal mass, circular binary, the secular orbital evolution rate is given by

$$\frac{\dot{a}}{a_B} = 8 \left(\frac{l_0}{\Omega_B a_B^2} - \frac{3}{8} \right) \frac{\dot{M}}{M_B}, \quad (40)$$

where the total torque per unit of accreted mass is

$$l_0 = \langle j_{\text{tot}} \rangle / \langle \dot{M} \rangle. \quad (41)$$

Therefore, whether binary shrink or expand depends on whether l_0 is greater or smaller than $3\Omega_B a_B^2/8$.

To quantify the evolution of the disc morphology, we also calculate the mass-weighted eccentricity of the cavity

$$\langle e \rangle_x = \frac{\int_{a_B}^{6a_B} \int_0^{2\pi} e_x \Sigma r dr d\phi}{\int_{a_B}^{6a_B} \int_0^{2\pi} \Sigma r dr d\phi}, \quad (42)$$

$$\langle e \rangle_y = \frac{\int_{a_B}^{6a_B} \int_0^{2\pi} e_y \Sigma r dr d\phi}{\int_{a_B}^{6a_B} \int_0^{2\pi} \Sigma r dr d\phi}, \quad (43)$$

where the eccentricity vector and its the x, y component are

$$\mathbf{e} = \frac{v^2 \mathbf{r} - (\mathbf{v} \cdot \mathbf{r}) \mathbf{v}}{GM_B} - \hat{\mathbf{r}}, \quad (44)$$

$$e_x = \frac{rv_r v_\phi}{GM_B} \sin \phi + \left(\frac{rv_\phi^2}{GM_B} - 1 \right) \cos \phi, \quad (45)$$

$$e_y = -\frac{rv_r v_\phi}{GM_B} \cos \phi + \left(\frac{rv_\phi^2}{GM_B} - 1 \right) \sin \phi. \quad (46)$$

Similar to mass-weighted eccentricity, we calculate the mass dipole of the entire CBD.

$$\Psi = \int_0^{18a_B} \Sigma e^i \phi r dr d\phi, \quad (47)$$

where the upper limit of the integration is chosen to be the inner radius of the damping zone. The quantity monitors the growth and damping of any asymmetric instability in the CBD, including disc

eccentricity and spiral features. We also output 2D snapshots of various fluid quantities (such as surface density Σ , temperature T , viscosity ν , and the gravitational torque density $T_{\text{grav}}^{2D} = -\Sigma \mathbf{r} \times \nabla \Phi$ every 10 orbits.

2.6 Simulation Runs

We show in Table 1 the parameters and various specific torque components of all simulations presented in the main text of this paper. In the seven columns, we separately indicate (i) the ID representing the simulations, (ii) the type of viscosity profile, (iii) the type of equilibrium temperature profile, (iv) the cooling parameter β , (v) the specific accretion torque $\langle j_{\text{acc}} \rangle / \langle \dot{M} \rangle$, (vi) the specific gravitational torque $\langle j_{\text{grav}} \rangle / \langle \dot{M} \rangle$ and (vii) the specific total torque $\langle j_{\text{tot}} \rangle / \langle \dot{M} \rangle$. The IDs characterizing each run are in the form of $\mathbf{t-n-b-}$, including information of the type of temperature profile, viscosity profile and the value of cooling parameter β in the simulations. For convenience, we will refer to a certain subset of simulations using $\mathbf{t-n-b-}$. For example, we will first discuss the simulations employing type I viscosity profile and type I temperature profile in Section 3 and we use $\mathbf{t1n1b-}$ for short.

We separate our simulations into two sets: the fiducial runs and the parameter survey. The convergence tests of simulation resolution, grid configuration, and sink parameters are investigated thoroughly and will be reported in our follow-up work [Wang et al. \(2022a\)](#). The fiducial runs consists of two subsets of simulations separately adopting constant viscosity profile $\mathbf{t1n1b-}$ and α -viscosity profile $\mathbf{t1n3b-}$. Section 3 will be mainly based on these simulations.

As one of our goals of this study, we also include 4 additional subsets of simulations in the parameter survey to explore the impact of various temperature and viscosity profiles on binary orbital evolution. In the last two subsets of the simulations, we adopt fixed α -viscosity profile. Instead of varying locally as the simulation proceeds, the temperature/sound speed influencing the viscosity is set to the prescribed value based on the initial temperature. For clarity, these simulations have ID labeled with $*$ in the end: $\mathbf{t-n-b-*}$.

3 SIMULATION RESULTS

We separately discuss the combined effect of dynamical cooling and viscous heating on angular momentum transfer between the disc and the binary, accretion variability, and disc morphology. We first show the results using constant kinematic viscosity in Section 3.1, and then the results employing dynamically varying α -viscosity in Section 3.2. The major difference between the two choices is whether the viscosity will be affected by local temperature or not (namely, whether the viscosity profile is time-dependent). Through this approach, we can evaluate how the dependence of viscosity on temperature affects binary migration rate, morphology, and accretion variability. And as we will show in Section 3.3, simulations employing fixed α -viscosity behave similarly to those employing constant kinematic viscosity. Here we show the constant viscosity runs first in order to comparing with previous studies (e.g., [Duffell et al. 2020](#); [Dittmann & Ryan 2021](#)).

3.1 Results for Constant Viscosity

In this subsection we explore the accretion behaviour of CBDs with dynamical cooling and constant viscosity, along with the angular momentum transfer within the disc and between the disc and the binary.

ID	ν (Type)	T (Type)	β	$\langle \dot{J}_{\text{acc}} \rangle / \langle \dot{M} \rangle$	$\langle \dot{J}_{\text{grav}} \rangle / \langle \dot{M} \rangle$	$\langle \dot{J}_{\text{tot}} \rangle / \langle \dot{M} \rangle$
Fiducial Runs						
t1n1b0.0	Const (I)	I	0.0	0.251	0.458	0.709
t1n1b0.2			0.2	0.251	0.100	0.351
t1n1b0.5			0.5	0.250	-0.079	0.172
t1n1b1.0			1.0	0.249	-0.078	0.172
t1n1b2.0			2.0	0.248	0.033	0.281
t1n1b4.0			4.0	0.248	-0.738	-0.491
t1n3b0.0	α -visc (III)	I	0.0	0.253	0.506	0.759
t1n3b0.2			0.2	0.253	0.363	0.616
t1n3b0.5			0.5	0.253	-1.246	-0.993
t1n3b1.0			1.0	0.253	0.292	0.545
t1n3b2.0			2.0	0.252	0.535	0.786
t1n3b4.0			4.0	0.250	0.439	0.689
Parameter Survey						
t2n1b0.0	Const (I)	II	0.0	0.250	0.429	0.679
t2n1b0.2			0.2	0.250	0.093	0.344
t2n1b0.5			0.5	0.250	-0.078	0.173
t2n1b1.0			1.0	0.250	-0.161	0.089
t2n1b2.0			2.0	0.250	-0.086	0.164
t2n1b4.0			4.0	0.250	-0.525	-0.276
t2n2b0.0	α -visc (II)	II	0.0	0.250	0.505	0.756
t2n2b0.2			0.2	0.260	0.371	0.631
t2n2b0.5			0.5	0.271	-1.989	-1.719
t2n2b1.0			1.0	0.261	0.074	0.335
t2n2b2.0			2.0	0.258	0.177	0.434
t2n2b4.0			4.0	0.259	0.311	0.571
t1n3b0.0*	Fixed α -visc (III)	I	0.0	0.251	0.471	0.722
t1n3b0.2*			0.2	0.251	0.278	0.529
t1n3b0.5*			0.5	0.251	0.178	0.429
t1n3b1.0*			1.0	0.251	0.119	0.371
t1n3b2.0*			2.0	0.251	0.153	0.404
t1n3b4.0*			4.0	0.251	-0.167	0.084
t2n2b0.0*	Fixed α -visc (II)	II	0.0	0.250	0.505	0.756
t2n2b0.2*			0.2	0.250	0.326	0.577
t2n2b0.5*			0.5	0.250	0.226	0.477
t2n2b1.0*			1.0	0.250	0.163	0.413
t2n2b2.0*			2.0	0.250	0.136	0.386
t2n2b4.0*			4.0	0.250	-0.062	0.188

Table 1. Summary of simulation parameters and key results. All of the simulations included in this paper are presented. We have separated simulations to fiducial runs and parameter survey runs. Fiducial runs include two sets of simulations employing constant viscosity and α -viscosity, which are discussed in the Section 3. Parameter survey runs include four sets of simulations surveying the impact of different temperature profiles and viscosity prescriptions. Different from adopting standard α -viscosity, we adopt fixed α -viscosity in the last two subsets (labeled with *). The viscosity profiles in these simulations are set to prescribed values instead of varying with local temperature.

3.1.1 Angular Momentum Transfer

In the locally isothermal limit $\beta = 0$, the specific torque calculated from our simulation is in close agreement with the results obtained in previous works. The specific accretion torque and the gravitational torque are outputted as a time series. These quantities are then time-averaged in the interval of $[2000P_B, 2200P_B]$, after the disc has reached a quasi-steady state. We find the specific torque acting on the binary is

$$l_0 = \frac{\langle \dot{J}_{\text{tot}} \rangle}{\langle \dot{M} \rangle} \simeq 0.709 a_B^2 \Omega_B \quad (48)$$

which is similar to the result $l_0 = 0.729 a_B^2 \Omega_B$ obtained in [Dittmann & Ryan \(2021, 2022\)](#) in which a constant viscosity profile and the torque-free sink prescription are adopted.

We employed a second set of diagnostics, measuring different components of angular momentum current due to advection, viscosity and gravitational interaction as shown in Figure 2. The overlaid yellow horizontal dashed line representing the directly calculated specific torque onto the binary, is in close agreement with the specific angular momentum current represented by the orange line. Hence, we can see that the quasi-steady state of angular momentum transfer both between the disc and the binary and within the CBD is indeed reached.

Impact of dynamical cooling: Figure 3 shows the dependence

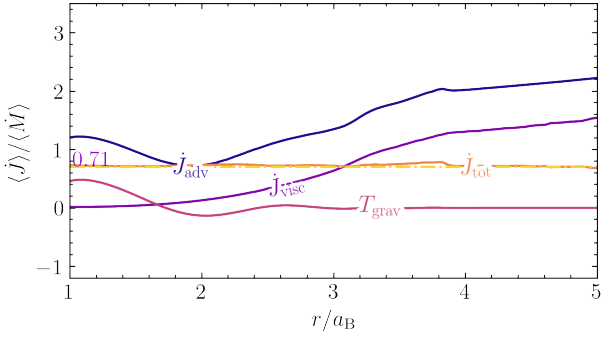


Figure 2. Radial distribution of the time-averaged advective, viscous, gravitational and total angular momentum current for Run $\mathbf{t1n1b0.0}$, with viscosity $\nu = 10^{-3} a_B^2 \Omega_B$ and locally isothermal equation of state. The orange curve is remarkably flat, showing that a quasi-steady state has been reached. For comparison purpose, we overlay a horizontal yellow dashed line with the value $\langle \dot{J}_{\text{tot}} \rangle = 0.709 \langle \dot{M} \rangle a_B^2 \Omega_B$.

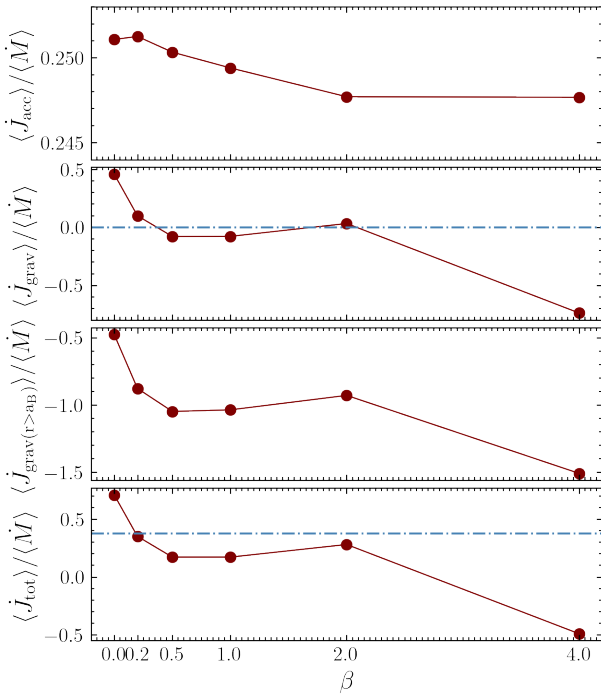


Figure 3. Various specific torque components and the total specific torque of the CBD acting on the binary as a function of parameterized cooling time β in fiducial run subset $\mathbf{t1n1b-}$. From the top to the bottom are (1) the specific accretion torque, (2) the specific gravitational torque, (3) the specific gravitational torque from the region $r > a_B$, and (4) the specific total torque. The dashed blue line in the second panel differentiates the sign of total gravitational torque, and the dashed line in the fourth panel illustrates the threshold of binary orbital evolution.

of these specific torque components and the total specific torque on cooling parameter β . As β becomes larger, the specific angular momentum transfer from the disc to the binary decreases, with a small-magnitude increase around $\beta = 2.0$. From the fourth panel of Figure 3, it is clear that the binary would experience inspiral when the equation of state deviates from locally isothermal. Tracing the origin of this dependence, we can separately analyze the contribution from each torque component: (i) The specific accretion torque is insensitive to the thermodynamics of the CBD. If the binary accretes isotropically, the specific angular momentum of the accreted gas should be the same as that of the binary: $l_B = q_B(1+q_B)^{-2} a_B^2 \Omega_B = 0.25 a_B^2 \Omega_B$

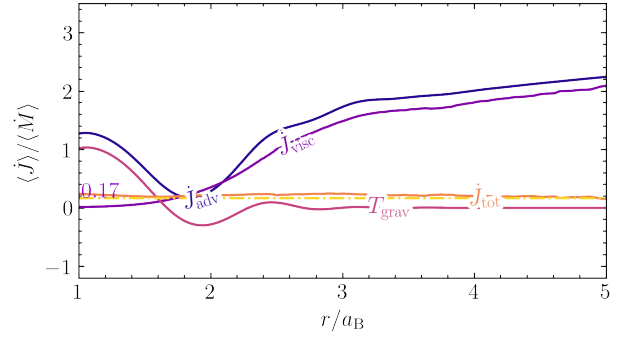


Figure 4. Similar to Figure 2, except for Run $\mathbf{t1n1b0.5}$, with cooling parameter $\beta = 1.0$. The gravitational and viscous angular momentum current T_{grav} and \dot{J}_{visc} are significantly larger compared to those in Figure 2, resulting in a significantly smaller total angular momentum current \dot{J}_{tot} .

(see Section 4.2 in Duffell et al. 2020). These small differences between the specific accretion torque and contributions from isotropic accretion originate from binary’s anisotropic accretion (see Section 2.2 in Muñoz et al. 2019 for a detailed explanation). (ii) The specific gravitational torque is the main cause of binary orbital inspiral. Comparing the results from the second and the fourth panels in Figure 3, we see that the gravitational torque outside $r = a_B$ is responsible for rapid change in total torques. This also suggests that in this simulation setup, the contribution from the mini-discs is insensitive to the cooling timescale.

Interpretation on binary orbital evolution: Figure 2 and 4 show the radial profiles of angular momentum current for $\beta \approx 0$ (locally isothermal) and 0.5. The former and the latter separately correspond to an outspiral and an inspiraling binary. The differences between the two are clear: when $\beta = 0.5$, the specific gravitational angular momentum current around $r = a_B$ and the specific viscous angular momentum current are larger, while the specific advection angular momentum current is comparable to the locally isothermal scenario. The same can be seen in the third panel of Figure 3, where the gravitational torque outside a_B is smaller when $\beta = 1.0$ comparing to $\beta = 0.0$. This can be credited to a shallower and smaller cavity when β is larger (as illustrated in Figure 6, see a further description in Section 3.1.3).

3.1.2 Accretion Variability

To explore the dependence of accretion variability on the cooling time, we keep track of the accretion rate onto each binary component 100 times per orbit. The power spectrum (left column) and the time series (right column) of accretion rate are shown in Figure 5, for $\beta \in [0.0, 0.2, 0.5, 1.0, 2.0, 4.0]$ from the top to the bottom. The power spectra are calculated using the time series of accretion rate in the last 200 orbits. They are also normalized by the largest amplitude to show the relative difference.

The magnitude of accretion variability and the characterized frequencies are the two features that we focus on here. (i) The accretion variability is not significantly suppressed with increasing β in simulations employing constant viscosity, unlike that of the simulations employing α -viscosity in Wang et al. (2022c) and Section 3.2.2. The variation of accretion rate is always around 25% – 50% of the average accretion rate. (ii) Except for the $\beta = 4.0$ case, the dominant variability frequency is about $\Omega_B/5$. This is widely acknowledged as the “lump-modulated” accretion variability (e.g., MacFadyen & Milosavljević 2008; D’Orazio et al. 2013; Miranda et al. 2017). There are also a series of other periodic variations with higher frequencies

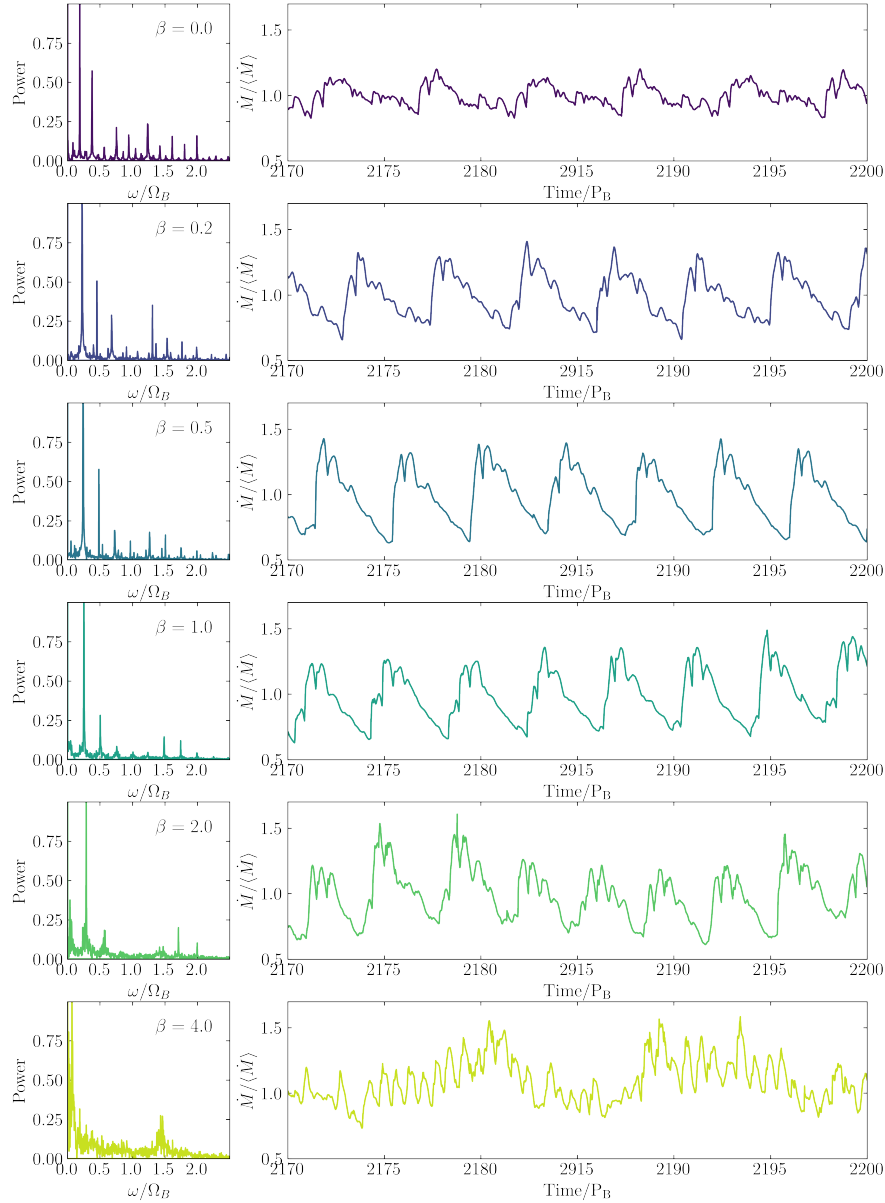


Figure 5. Accretion variability in the fiducial run subset **t1n1b-** with constant kinematic viscosity. The first column is the power spectrum of the total accretion rates and the right column is the time series of accretion rate in $2170P_B - 2200P_B$. From the top to the bottom, the value of cooling parameter β gradually increases following the sequence $[0.0, 0.2, 0.5, 1.0, 2.0, 4.0]$.

which can be seen in the power spectrum. These are also found in previous works (e.g., [Miranda et al. 2017](#)). The relatively large peak near the frequency of $\sim 2\Omega_B$ is related to the accretion streams carrying materials from the CBD to the mini-discs, which periodically repeat themselves every half of the binary orbit. The case of $\beta = 4.0$ is worth special care and we postpone the discussion to Section 3.1.4.

It is worth noting that, unlike specific torques, accretion variability calculated can be strongly dependent on sink prescriptions, including the type of the sink, sink radius, and sink timescale (as pointed out by [Farris et al. 2014](#), [Tang et al. 2017](#), [Duffell et al. 2020](#) and [Dittmann & Ryan 2021](#)). So the validity of our results in this section could be affected if a significantly different sink term is adopted.

3.1.3 Disc Morphology

Figure 6 shows a series of snapshots of disc surface density and temperature with increasing cooling timescale β from left to right. The binary’s gravitational tidal potential clears an eccentric low-density cavity, which is penetrated by narrow accretion streams characterized by azimuthal number $m = 1$ or 2. The high-density lump orbiting around the cavity wall is also prominent.

As β increases, the most significant changes occur in the shape and size of the cavity: the cavity gradually becomes “shallower” and more symmetric. These features are also reported in [Sudarshan et al. \(2022\)](#). “Shallower” cavity is also the signal that the gravitational torque truncates the CBD not as effectively as in the locally isothermal case. This results from a hotter cavity with larger β , which can be seen from the temperature profile in the lower panels. This trend of “a more symmetric cavity” is consistent with our findings in [Wang et al. \(2022c\)](#), despite the fact that in this work the “twisted spirals” are no

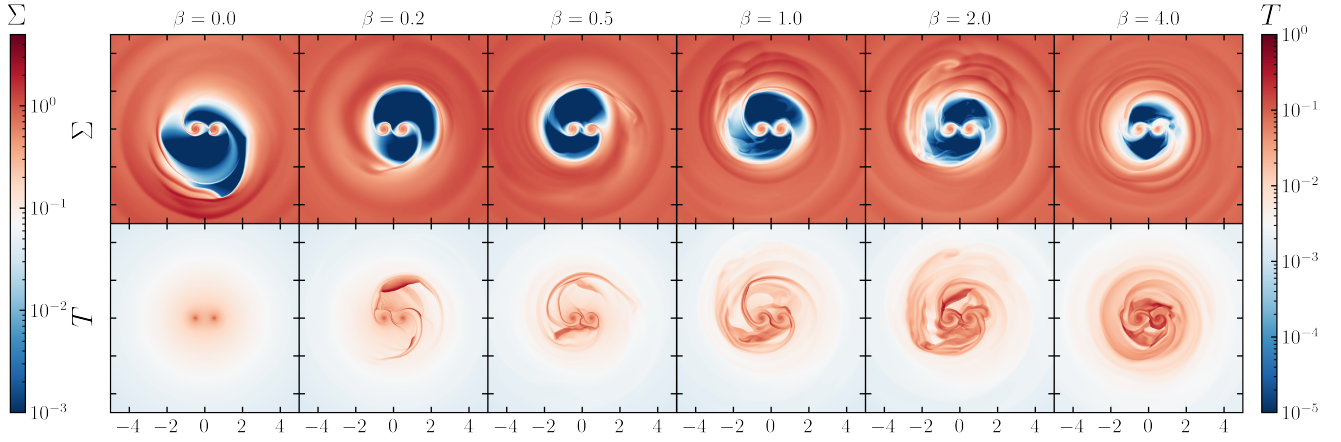


Figure 6. The density distribution (first row) and the temperature distribution (second row) in the fiducial run subset **t1n1b-** with constant kinematic viscosity. From the left to the right, the value of β increases.

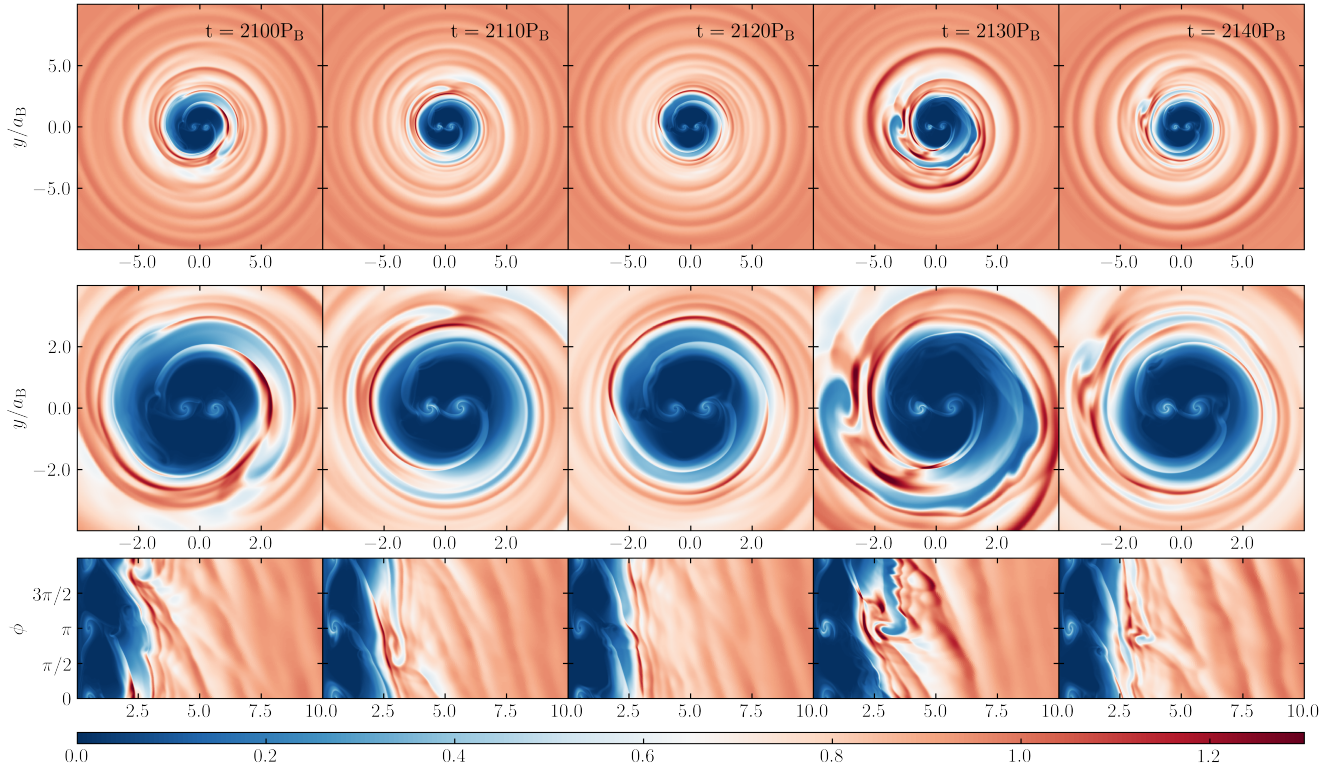


Figure 7. A series of snapshots with parameterized cooling time $\beta = 4.0$ in run **t1n1b4.0**. The upper two rows are the original simulation snapshots in cartesian geometry (x, y) while in the bottom row shows the interpolated density distribution in (r, ϕ) , in order to better illustrate the pitch angles of the spiral density waves. In the bottom panel, from the 3rd column to the right, it can be seen that multiple density peaks appear in the inner radial range of $[2.0a_B, 4.0a_B]$ and the outer radial range of $[3.0a_B, 10.0a_B]$. In the 4th column, only single density peak appears both the inner region and the outer region. Other figures show the gradual transition from the single-armed spiral to two-armed spirals.

longer present. The absence of “twisted spirals” could be originated from the choice of constant viscosity.

3.1.4 Quasi-Periodic Variation (QPV) in Morphology

We found in Run **t1n1b4.0** with $\beta = 4.0$, the disc morphology exhibits quasi-periodic variability (QPV, for short). Shown in Figure 7, QPV can be regarded as a periodic transition of disc morphology from single-armed spiral density waves to two-armed spiral density waves. Since this transition happens in different scales simultaneously, we show the density snapshots at

$[2100, 2110, 2120, 2130, 2140]P_B$ of the CBD ($r < 10a_B$) in the first row of Figure 7 and the zoom-in figure in the second row. At a certain time, there exists either a large spiral structure spanning from $\sim 2a_B$ to $\sim 10a_B$ and lopsided accretion streams in the disc cavity; or larger-scale two-armed spirals far from the binary and tightly-wounded two-armed accretion streams at the cavity wall. It is worth noticing that the large-scale spiral features are not present in the locally isothermal simulations. The first row of Figure 7 shows that the density waves propagate far from the binary, unlike the density waves dissipate severely within $\sim 5a_B$ in the locally isothermal case (see, e.g., [Miranda et al. 2017](#)).

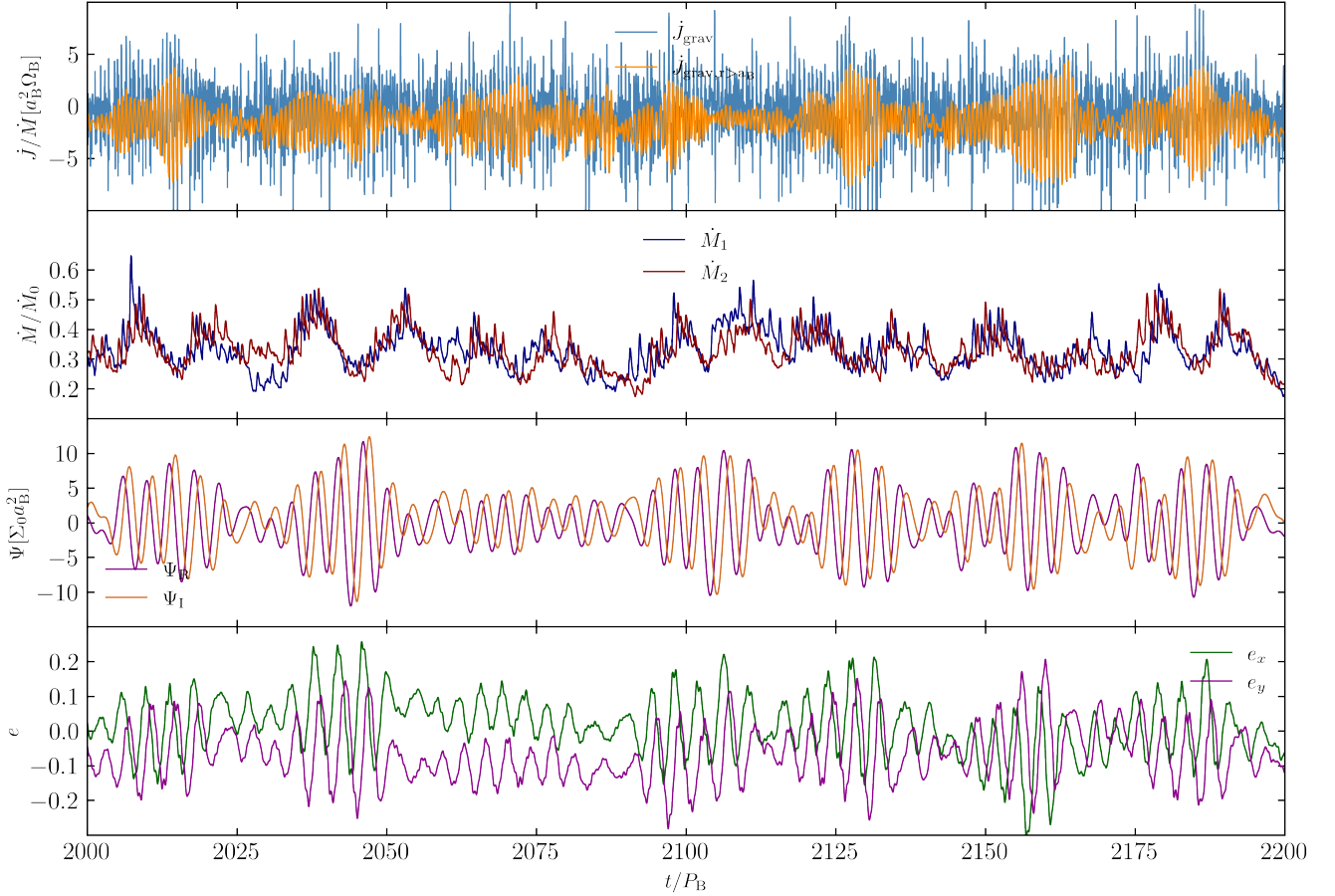


Figure 8. Variability of different diagnostics in fiducial run **t1n1b4.0** in the period of $[2000, 2200]P_B$. From the top to the bottom are (i) the specific angular momentum transfer rate due to gravitational interaction \dot{J}_{grav} , (ii) the accretion rate onto each component of the binary \dot{M} , (iii) the mass dipole of the CBD Ψ , and (iv) the mass-weighted eccentricity of the cavity e . The QPV feature is most prominent in the last two panels. The calculated mass dipole and eccentricity have the maximum magnitudes when the single-armed spiral is present and have the minimum magnitudes when the two-armed spirals are present.

The large-scale density waves are generated or strengthened by the stream crossing in the vicinity of the binary (similar to Mösta et al. 2019). This is one possible reason for the coexistence of different scale spiral features: (i) As illustrated in the leftmost panels, the accretion streams connecting to the mini-discs are merged to form a “lump”-like structure at the cavity wall. And this lump can drive the single-armed spiral formation in the large scale. (ii) When the morphology in the disc cavity is symmetric, the lump at the cavity wall is replaced by two-armed, tightly wound spiral density waves. The absence of the lump lead to more symmetric structure in the large scale as well. This quasi-periodic variability has a period of $\sim 30P_B$ as shown in Figure 5, 7, and 8.

The existence of this quasi-periodic variability has a large impact on accretion variability and angular momentum transfer between the disc and the binary. The panels in Figure 8 show the rate of specific angular momentum transfer from the CBD to the binary, accretion rate onto each binary component, mass quadrupole of the disc and the mass-weighted eccentricity of the cavity in the period of $[2000, 2200]P_B$. There exists a clear correlation between these four quantities. Especially, the mass accretion rate exhibits long-term variability, which is not reported in the previous 2D hydrodynamical simulations.

Perhaps more curiously, similar features have been reported in 3D MHD simulations of Shi & Krolik (2015), which use a globally isothermal equation of state with sound speed $0.1\Omega_B a_B$, and with

viscosity provided by MRI turbulence. And our simulations that employ dynamically varying α -viscosity, which will be discussed in Section 3.2, show similar features when the disc is hot enough ($\beta = 4.0$). Further work is needed investigate the origin of this phenomenon.

3.2 Results for Dynamically Varying Viscosity

Similar to Section 3.1, we follow our standard suite of analysis for the simulation subset **t1n3b-** with dynamically varying α -viscosity. In this series of runs, the viscosity profile is dynamically influenced by the temperature profile, which is set by the balance between viscous heating and β -cooling. Several differences are expected: with higher temperature in the cavity and consequently larger viscosity, the disc self-adjusts faster towards a quasi-steady state. It further influences the angular momentum transfer and binary’s accretion variability.

3.2.1 Angular Momentum Transfer and disc Morphology

Again, we summarize the dependence of various specific torque components on the cooling parameter β in Figure 9. The total angular momentum current per unit mass through the CBD in the locally isothermal limit is illustrated in Figure 11, in which case the specific

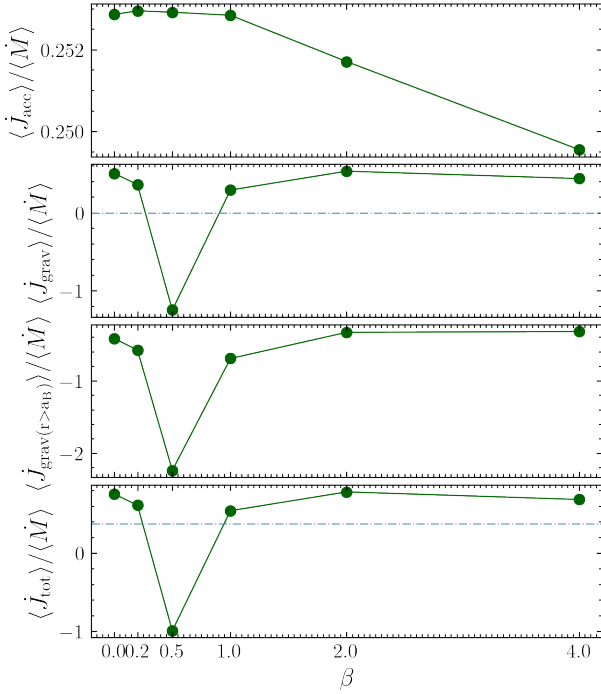


Figure 9. Same as Figure 3, with the four panels showing how different torque components and the total torque vary with β in fiducial run subset $\mathbf{t1n3b-}$ (with dynamically varying viscosity).

total torque is given by

$$\frac{\langle \dot{J}_{\text{tot}} \rangle}{\langle \dot{M} \rangle} \approx 0.759 a_B^2 \Omega_B \quad (49)$$

This value is close to the result for the constant-viscosity case (Equation 48), and similar to Dittmann & Ryan (2022) ($l_0 = 0.767 a_B^2 \Omega_B$) and is somewhat larger than the result ($l_0 = 0.723 a_B^2 \Omega_B$) of Moody et al. (2019). The differences result from the choice of torque-free sink prescription.

Impact of dynamical cooling: From Figure 9, we see that the angular momentum transfer between the disc and the binary depends on β in a non-monotonic way, with the minimum of $\langle \dot{J}_{\text{tot}} \rangle / \langle \dot{M} \rangle$ achieved at $\beta = 0.5$. This trend is similar to our previous findings in Wang et al. (2022c). Similar to Section 3.1, it is useful to decompose the total specific torque to accretion torque and gravitational torque. We find: (i) The specific accretion torque is insensitive to the thermodynamics, with a smaller variation compared to the case with constant viscosity; the specific accretion torque is very close to the specific torque of the binary $l_B = 0.25 a_B^2 \Omega_B$. (ii) The specific gravitational torque, and more specifically, the gravitational torque outside of $r = a_B$, is responsible to the “v” shape transition as β increases.

Interpretation on binary orbital evolution: From the morphology of the runs shown in Figure 10, it is easy to notice a prominent transition in the CBD cavity from eccentric to circular when β changes from 0.2 to 1.0. When $\beta = 0.5$ (the third column in Figure 10), the disk materials at the edge of the cavity wall exhibit “twisted” features and leave a trailing spiral extending to $r \approx 5a_B$. The CBD morphology is fixed while the accretion streams in the cavity provide the only remaining variability. As β increases further, the morphology of both the CBD and the accretion streams roughly stay fixed and their patterns corotate with the binary: the cavity is penetrated by two-armed, tidally induced spirals directly connecting the binary and the CBD. The reason for the “v” shaped relation in the angular momentum transfer rate is qualitatively similar to our explanation in

Wang et al. (2022c): From Figure 9, we see that the major variation in total gravitational torques is originated from the region $r > a_B$, which means that it is the contribution from the accretion streams in the cavity and the outer CBD that sensitively depends on the cooling time. Meanwhile, we show the radial dependence of different angular momentum current components of run $\mathbf{t1n3b0.5}$ (corresponding to the case of binary inspiral in Figure 9) in Figure 12. We see that the angular momentum current from gravitational interaction increases significantly in the radial range of $[1.0, 1.7]a_B$, which corresponds to the location of accretion streams connecting the binary and the CBD. The specific angular momentum current due to viscous transport is also larger than that due to advection. Therefore, the “v” shaped feature in Figure 9 likely stems from the cavity’s morphology transitioning from eccentric to circular. It is worth noticing that the specific angular momentum transfer rate onto the binary (yellow dash-dotted line) deviates from that across the CBD (orange solid line) in run $\mathbf{t1n3b0.5}$ as shown in Figure 12. The difference is most likely resulted from the contribution from pressure and the finite size of the sink cell (see, e.g., Li & Lai 2022).

3.2.2 Accretion Variability

Similar to the results reported in Section 3.1.2, we analyze the accretion behaviour of the binary. The normalized power spectrum (left column) and the time series (right column) are shown in Figure 13.

We first focus on the magnitude of accretion variability. It is clear that as β increases from 0.0 to 2.0 (from top to bottom), the magnitude of accretion rate variability is gradually suppressed. This result is consistent with our findings in Wang et al. (2022c). The suppression in accretion variability could be traced back to the suppression of variability in the disc morphology shown in Figure 10.

The characterized frequencies of accretion variability has a complex dependence on β . When β is small (i.e., $\beta = [0.0, 0.2]$), the accretion behaviour is similar to the locally isothermal case: There are two characteristic frequencies: the “lump”-induced, relatively long-term accretion variability at about $\Omega_B/5$, and the variability related to the binary orbital motion and motion of the accretion streams at $2\Omega_B$. When $\beta = 0.5$, the only dominant frequency is $\sim 1.3\Omega_B$. This is also similar to our previous results (Wang et al. 2022c). The high-density lump disappears and the dominant frequency is associated with the spiral accretion streams. When $\beta \gtrsim 1.0$, the accretion process is much more stable, corresponding to the transition in disc morphology at $\beta = 1.0$ shown in Figure 10. Materials are directly transferred from CBD to the binary through the two-armed spirals. We also note that the accretion variability could depend on the sink prescription. This is because the CBD is in phase corotating with the binary and the variabilities associated with the disc morphology changes are efficiently suppressed.

Similar to the constant-viscosity simulations, it is worth noticing that the magnitude of the accretion variability is larger for $\beta = 4.0$ than for $\beta = 2.0$. The prominent frequency that characterizes this variability is similar to that found in Section 3.1.4. This shows that quasi-periodic variability also exists in simulations $\mathbf{t1n3b-}$ adopting dynamically varying α -viscosity.

3.3 Discussion: Parameter Survey

Our results presented in section 3.1 and 3.2 are based on the two subsets of the simulations in the fiducial runs. Here we discuss additional results included in the parameter survey in Table 1. There are 4 subsets of simulations: (i) $\mathbf{t2n2b-}$, with axisymmetric (equilibrium) temperature profile and axisymmetric, dynamically varying

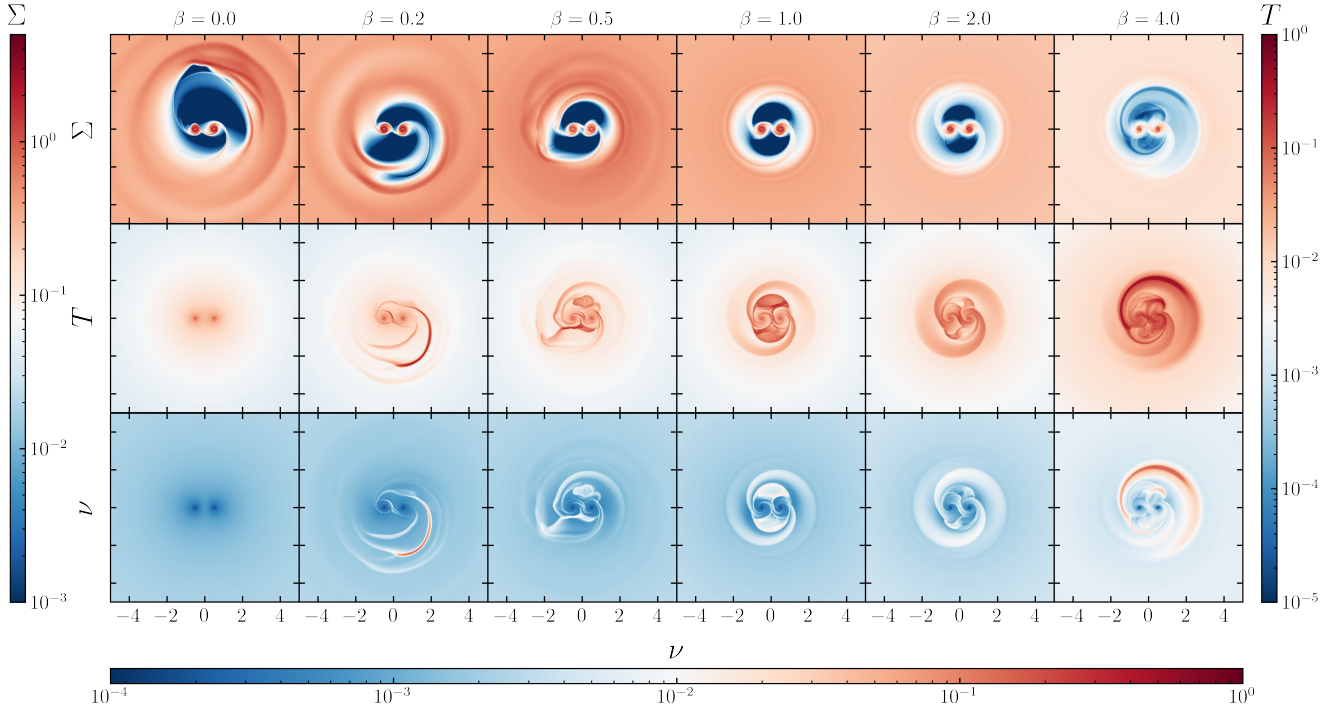


Figure 10. Similar to Figure 6, showing the density distribution (first row), the temperature distribution (second row) and the viscosity distribution (third row) in the fiducial run subset t1n3b- with dynamically varying α -viscosity.

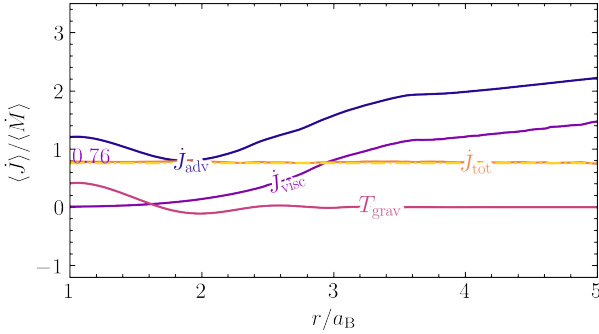


Figure 11. Similar to Figure 2, but using the dynamically varying α -viscosity. The corresponding simulation ID is t1n3b0.0.

α -viscosity; (ii) t2n1b-, with axisymmetric temperature profile and constant viscosity; (iii) t1n3b-*, with the temperature profile centered on each component of the binary and fixed α -viscosity; and (iv) t2n2b-*, with axisymmetric temperature profile and axisymmetric fixed α -viscosity. We can categorize the 4 different subsets along with 2 in the fiducial runs into two types: (i) simulations having a fixed viscosity profile or (ii) a dynamically varying viscosity profile. The former includes t1n1b-, t2n1b-, t1n3b-*, and t2n2b-*, while the latter includes t1n3b- and t2n2b-. As we will show below, similar dependences between the properties, including CBD morphology and angular momentum transfer rate, and cooling time β are found within each category.

We show the inner CBD morphology, temperature distribution (and viscosity distribution) if adopting dynamically varying α -viscosity) in the 2nd (3rd) rows of each subset in Figure A1, A2, A3 and A4 corresponding to run t2n1b-, t2n2b-, t1n3b-* and t2n2b-*. For simulations adopting a fixed viscosity profile, as the cooling time β increases, the CBD cavity gradually becomes shallower and more circular. Meanwhile, the high-density lump at

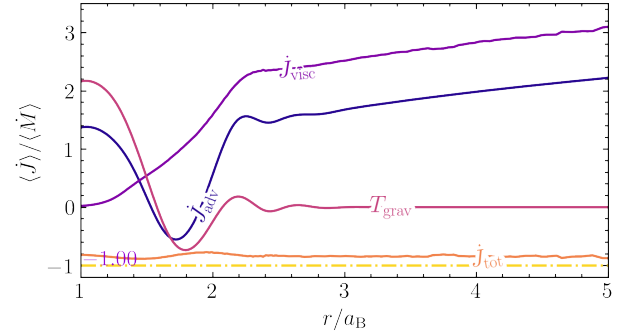


Figure 12. Similar to Figure 11, but with cooling parameter $\beta = 0.5$. In comparison to Figure 11, the gravitational torque and viscous torque are significantly larger, resulting in a significantly smaller total angular momentum current. The corresponding simulation ID is t1n3b0.5.

the cavity wall gradually becomes a series of spirals. The temperature inside the CBD cavity also increases with increasing β . The morphology of temperature distribution becomes more closely coupled to the surface density profile. When $\beta = 4.0$, a quasi-periodic variability as described in Section 3.1.4 always appears. For simulations adopting a dynamically varying α -viscosity, the CBD cavity quickly circularize as β increases and the CBD has the same pattern speed as the rotating speed of the binary. When the inner disc is hot enough, the corotating disc pattern breaks up and the disc again becomes asymmetric/eccentric, at the same time exhibiting quasi-periodic variability. This can be originated from the fact that eccentric modes in the CBD are efficiently damped when the cooling timescale is close to local Keplerian timescale. We will analyse this effect analytically in Wang et al. (2022b).

Whether or not employing a fixed viscosity profile also significantly influences the dependence of the rate of angular momentum transfer from the disc to the binary on cooling time β . As illustrated

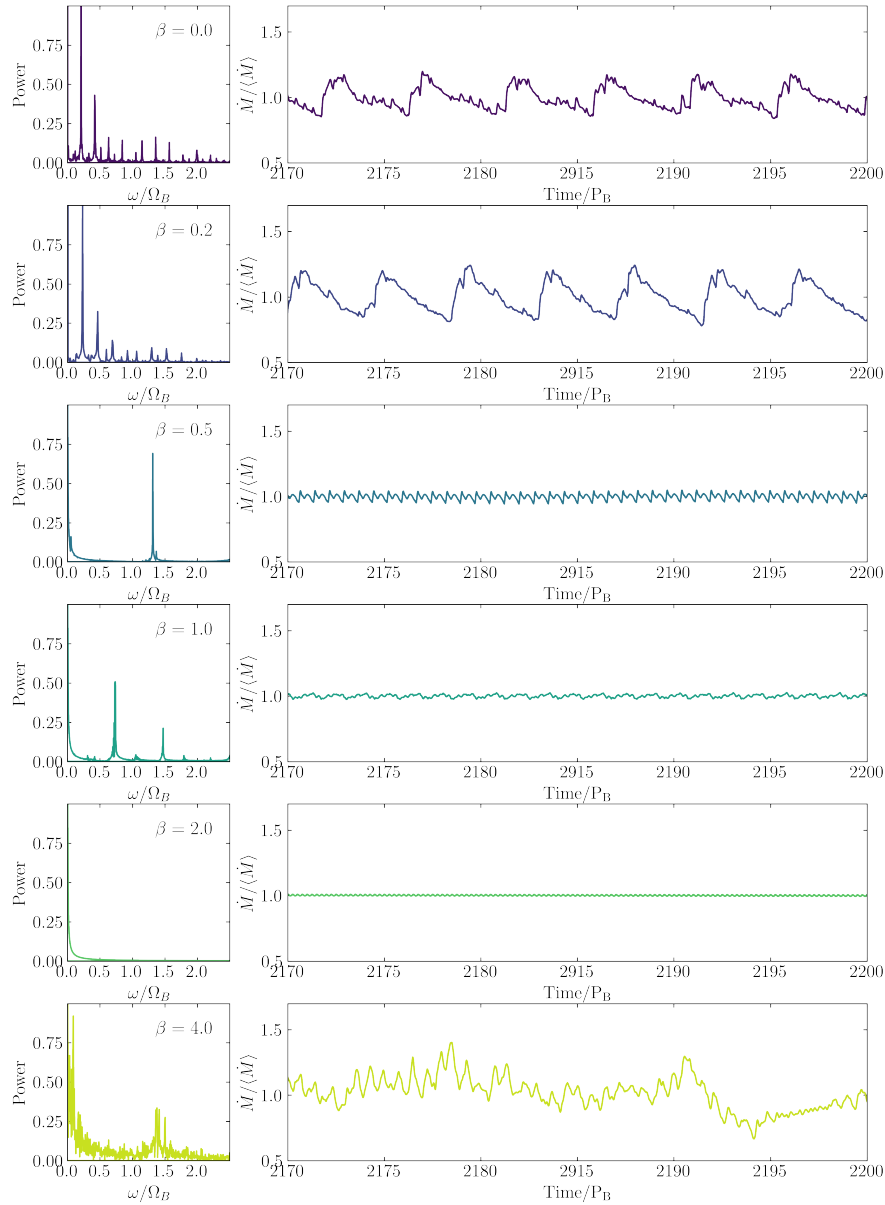


Figure 13. Similar to Figure 5, showing the accretion variability in the fiducial run subset t1n3b- with dynamically varying α -viscosity.

in Figure A5, when adopting a fixed viscosity profile, as the cooling time becomes longer, the angular momentum transfer rate from the disc to the binary gradually decreases. In the cases employing a dynamically varying α -viscosity, the dependence between the angular momentum transfer rate and the cooling time exhibit non-monotonic, “v”-shaped relation, as discussed in Section 3.1.1.

By showing the dependence of various diagnostics on cooling time, we find that although different choices of temperature and viscosity profiles can affect the details of the results, the overall trend of this dependence can be simply categorized into two kinds. This parameter survey shows that our results introduced in Section 3.1 and 3.2 are not artifacts of specific temperature and viscosity choices: it is a general result that whether or not explicitly including local temperature in viscosity profile will determine the dependence of the disc properties and the angular momentum transport on the cooling time.

4 SUMMARY

In this work, we have conducted a suite of 2D hydrodynamical simulations of circumbinary accretion in cartesian geometry, focusing on the impacts of viscous heating and dynamical cooling of the gas. We limit our study to equal mass binaries on fixed circular orbits at the center of CBDs with the (equilibrium) disc aspect ratio $h = 0.1$. To separate the effect of viscous heating and dynamical cooling, we conducted simulations with static, constant kinematic viscosity, and dynamically varying α -viscosity. The simulation results are discussed concentrating on the angular momentum transfer between the disc and the binary, the accretion variability and the disc morphology. This work is the extension of our recent paper (Wang et al. 2022c), which studied the same problem in a cylindrical coordinate and excised the central simulation domain ($r < a_B$).

Same as Wang et al. (2022c), our simulations use idealized treatment of thermodynamics by assuming cooling time t_{cool} to be a constant fraction of the local dynamical timescale. All of our simu-

lations have reached a quasi-steady state, such that the time-averaged mass flux and angular momentum flux across the CBD equal the mass and angular momentum transfer rates to the binary. The key results of our simulations are summarized below. Perhaps most importantly, we found that when the CBD's equation of state deviates from the locally isothermal limit, all results can sensitively depend on the viscosity prescription, especially whether the viscosity profile is fixed or dynamically varying with local temperature.

(i) Angular momentum transfer: As the parameterized cooling timescale β increases, the specific angular momentum transferred from the disc to the binary generally decreases when adopting constant viscosity (see Figure 3); even a slight deviation from the locally isothermal limit (i.e., $\beta = 0.2$) could result in orbital inspiral. When adopting the dynamically varying α -viscosity, the specific angular momentum received by the binary depends non-monotonically on β . Similar to our previous work (Wang et al. 2022c), for most β -values, the binary will experience orbital expansion; the binary could shrink in a small window around $\beta \approx 0.5$.

(ii) Accretion variability: As the cooling time becomes longer, the magnitude and characterized frequencies of accretion variability are barely affected when employing constant viscosity (see Figure 5). When employing α -viscosity, the accretion variability will be gradually suppressed as β increases (see Figure 13). On the other hand, when $\beta = 4.0$, the magnitude of the accretion variability is similar to the locally isothermal limit, and exhibits quasi-periodic features with a period of $\sim 30P_B$ (see Figure 8).

(iii) Disc Morphology: With a longer cooling time, the morphology of the inner disc generally becomes more symmetric. When adopting α -viscosity, the disc exhibits a transition at $\beta \approx 1.0$ from the morphology similar to the locally isothermal case to a fixed pattern corotating with the binary. But when the inner disc is hot enough (i.e., $\beta = 4.0$), the disc will exhibit quasi-periodic variability with a period of $\sim 30P_B$.

Comparing with our recent work (Wang et al. 2022c), we have made a large improvement in this work by resolving the region within the binary cavity. There are several obvious caveats of work. Firstly, we focus on CBDs with “equilibrium” disc aspect ratio $h = 0.1$ and equal-mass, circular binaries. The orbital evolution of the binary can sensitively depend on other binary or disc parameters. Secondly, our simulations are carried out in 2D. Only 3D hydrodynamical simulations can capture the possible deflection of density waves perpendicular to the disc midplane. More importantly, 3D MHD simulations which capture MRI turbulence can provide information regarding binary orbital evolution more realistically. Finally, our treatment of the thermodynamics of the gas is still over-simplified. We will aim to include radiative cooling and potentially radiation transport to attain a more realistic picture of CBD accretion.

ACKNOWLEDGEMENTS

We thank Gordon Ogilvie for helpful discussion. We also thank the KITP program “Bridging the Gap: Accretion and Orbital Evolution in Stellar and Black Hole Binaries” for helpful communications. This work is supported by the Dushi fund at Tsinghua University, and in part by the National Science Foundation under Grant No. NSF PHY-1748958. Numerical simulations are conducted in the Orion cluster at Department of Astronomy, Tsinghua University, and in TianHe-3 (A) at National Supercomputer Center in Tianjin, China.

DATA AVAILABILITY

The inclusion of a Data Availability Statement is a requirement for articles published in MNRAS. Data Availability Statements provide a standardised format for readers to understand the availability of data underlying the research results described in the article. The statement may refer to original data generated in the course of the study or to third-party data analysed in the article. The statement should describe and provide means of access, where possible, by linking to the data or providing the required accession numbers for the relevant databases or DOIs.

REFERENCES

- Armitage P. J., Natarajan P., 2002, *ApJ*, **567**, L9
 Begelman M. C., Blandford R. D., Rees M. J., 1980, *Nature*, **287**, 307
 Bertin E., Arnouts S., 1996, *A&AS*, **117**, 393
 Bonnell I. A., Bate M. R., 1994a, *MNRAS*, **269**, L45
 Bonnell I. A., Bate M. R., 1994b, *MNRAS*, **271**, 999
 Boss A. P., 1986, *ApJS*, **62**, 519
 D’Orazio D. J., Duffell P. C., 2021, *ApJ*, **914**, L21
 D’Orazio D. J., Haiman Z., MacFadyen A., 2013, *MNRAS*, **436**, 2997
 Dempsey A. M., Muñoz D., Lithwick Y., 2020, *ApJ*, **892**, L29
 Dittmann A. J., Ryan G., 2021, *ApJ*, **921**, 71
 Dittmann A. J., Ryan G., 2022, *MNRAS*, **513**, 6158
 Duffell P. C., D’Orazio D., Derdzinski A., Haiman Z., MacFadyen A., Rosen A. L., Zrake J., 2020, *ApJ*, **901**, 25
 Dutrey A., Guilloteau S., Simon M., 1994, *A&A*, **286**, 149
 Escala A., Larson R. B., Coppi P. S., Mardones D., 2005, *ApJ*, **630**, 152
 Farris B. D., Duffell P., MacFadyen A. I., Haiman Z., 2014, *ApJ*, **783**, 134
 Franchini A., Sesana A., Dotti M., 2021, *MNRAS*, **507**, 1458
 Frank J., King A. R., Raine D. J., 1985, *Accretion power in astrophysics*
 Gammie C. F., 2001, *ApJ*, **553**, 174
 Goldreich P., Tremaine S., 1979, *ApJ*, **233**, 857
 Haiman Z., Kocsis B., Menou K., 2009, *ApJ*, **700**, 1952
 Hamers A. S., Cai M. X., Roa J., Leigh N., 2018, *MNRAS*, **480**, 3800
 Heath R. M., Nixon C. J., 2020, *A&A*, **641**, A64
 Jaffe A. H., Backer D. C., 2003, *ApJ*, **583**, 616
 Kelley L. Z., Blecha L., Hernquist L., 2017, *MNRAS*, **464**, 3131
 Kley W., Haghighipour N., 2014, *A&A*, **564**, A72
 Kley W., Haghighipour N., 2015, *A&A*, **581**, A20
 Kley W., Thun D., Penzlin A. B. T., 2019, *A&A*, **627**, A91
 Kratter K. M., Matzner C. D., Krumholz M. R., 2008, *ApJ*, **681**, 375
 Lai D., Muñoz D. J., 2022, arXiv e-prints, p. arXiv:2211.00028
 Li R., Lai D., 2022, *MNRAS*, **517**, 1602
 MacFadyen A. I., Milosavljević M., 2008, *ApJ*, **672**, 83
 Mathieu R. D., Stassun K., Basri G., Jensen E. L. N., Johns-Krull C. M., Valenti J. A., Hartmann L. W., 1997, *AJ*, **113**, 1841
 Miranda R., Muñoz D. J., Lai D., 2017, *MNRAS*, **466**, 1170
 Moody M. S. L., Shi J.-M., Stone J. M., 2019, *ApJ*, **875**, 66
 Mösta P., Taam R. E., Duffell P. C., 2019, *ApJ*, **875**, L21
 Muñoz D. J., Lai D., 2016, *ApJ*, **827**, 43
 Muñoz D. J., Miranda R., Lai D., 2019, *ApJ*, **871**, 84
 Muñoz D. J., Lai D., Kratter K., Miranda R., 2020, *ApJ*, **889**, 114
 Mutter M. M., Pierens A., Nelson R. P., 2017, *MNRAS*, **465**, 4735
 Noble S. C., Mundim B. C., Nakano H., Krolik J. H., Campanelli M., Zlochower Y., Yunes N., 2012, *ApJ*, **755**, 51
 Noble S. C., Krolik J. H., Campanelli M., Zlochower Y., Mundim B. C., Nakano H., Zilhão M., 2021, *ApJ*, **922**, 175
 Penzlin A. B. T., Kley W., Nelson R. P., 2021, *A&A*, **645**, A68
 Penzlin A. B. T., Kley W., Audiffren H., Schäfer C. M., 2022, *A&A*, **660**, A101
 Sesana A., Vecchio A., Colacino C. N., 2008, *MNRAS*, **390**, 192
 Shakura N. I., Sunyaev R. A., 1973, *A&A*, **500**, 33
 Shi J.-M., Krolik J. H., 2015, *ApJ*, **807**, 131
 Stone J. M., Tomida K., White C. J., Felker K. G., 2020, *ApJS*, **249**, 4

- Sudarshan P., Penzlin A. B. T., Ziampras A., Kley W., Nelson R. P., 2022, [A&A, 664, A157](#)
- Tang Y., MacFadyen A., Haiman Z., 2017, [MNRAS, 469, 4258](#)
- Thun D., Kley W., 2018, [A&A, 616, A47](#)
- Tiede C., Zrake J., MacFadyen A., Haiman Z., 2020, [ApJ, 900, 43](#)
- Tobin J. J., et al., 2016, [Nature, 538, 483](#)
- Wang H., Lai D., Bai X., 2022b, in prep
- Wang H., Lin D. N. C., Bai X., Lai D., 2022a, in prep
- Wang H., Bai X., Lai D., 2022c, arXiv e-prints, p. [arXiv:2212.04199](#)
- Wyithe J. S. B., Loeb A., 2003, [ApJ, 590, 691](#)
- Zrake J., Tiede C., MacFadyen A., Haiman Z., 2021, [ApJ, 909, L13](#)
- d’Ascoli S., Noble S. C., Bowen D. B., Campanelli M., Krolik J. H., Mewes V., 2018, [ApJ, 865, 140](#)

APPENDIX A: PARAMETER SURVEY: TEMPERATURE PROFILE AND VISCOSITY PRESCRIPTION

In this appendix, we include the surface density, temperature and viscosity profiles (Figure [A1](#), [A2](#), [A3](#), and [A4](#)) of all the parameter survey subsets referred in Table [1](#): `t2n1b-`, `t2n2b-`, `t1n3b-*`, and `t2n2b-*`. Only the simulations in subset `t2n2b-` are employing viscosity which depends on local temperature. Though having different temperature and viscosity profile comparing to fiducial run subset `t1n3b-` (detailedly discussed in Section [3](#)), a dynamically varying viscosity makes there two subsets of simulations behave similarly: The shape of the cavity first changes from eccentric to circular, then changes to eccentric again with a longer cooling time. The temperature and viscosity in the CBD cavity also increase correspondingly. Simulations from all the other subsets have fixed viscosity profile in the comoving frame of the binary. And the resulting surface density and temperature distributions of these simulations are qualitatively similar: The shape of the CBD cavity generally changes from eccentric to circular as the cooling time increases. The temperature inside the cavity also rises with a longer cooling time.

This paper has been typeset from a \LaTeX file prepared by the author.

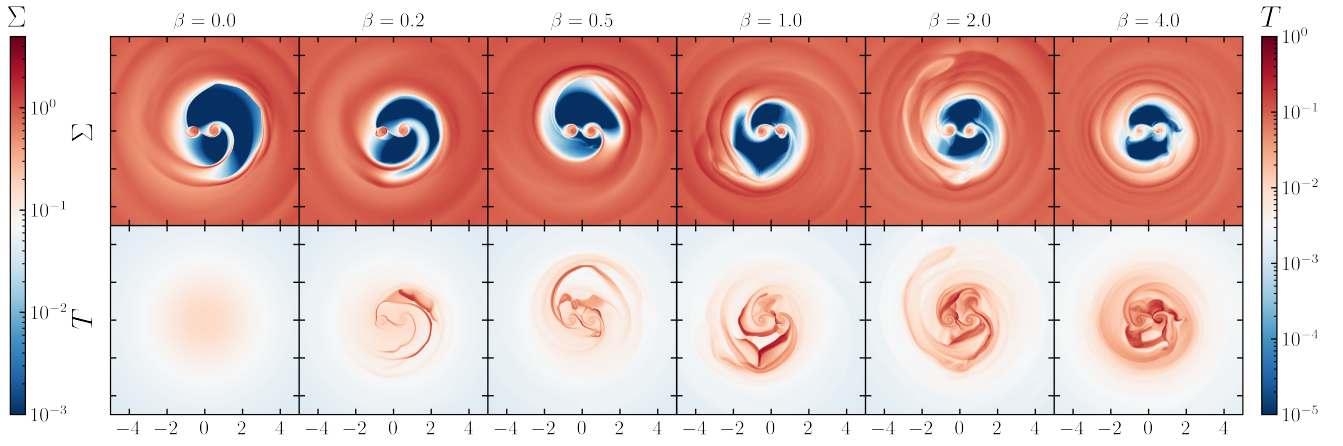


Figure A1. Similar to Figure 6, the density distribution (first row) and the temperature distribution (second row) in parameter survey subset t2n1b- with constant kinematic viscosity.

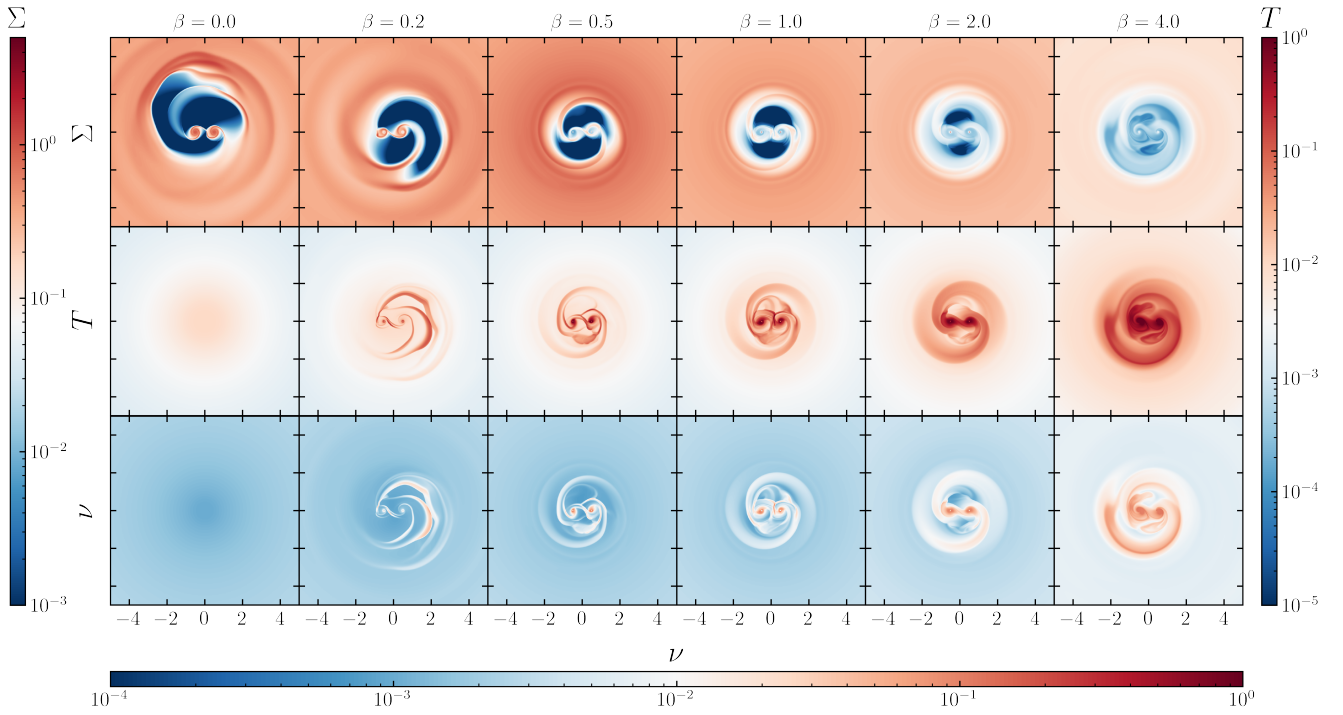


Figure A2. Similar to Figure 10, the density distribution (first row), the temperature distribution (second row) and the viscosity distribution (third row) in parameter survey subset t2n2b- with dynamically varying α -viscosity.

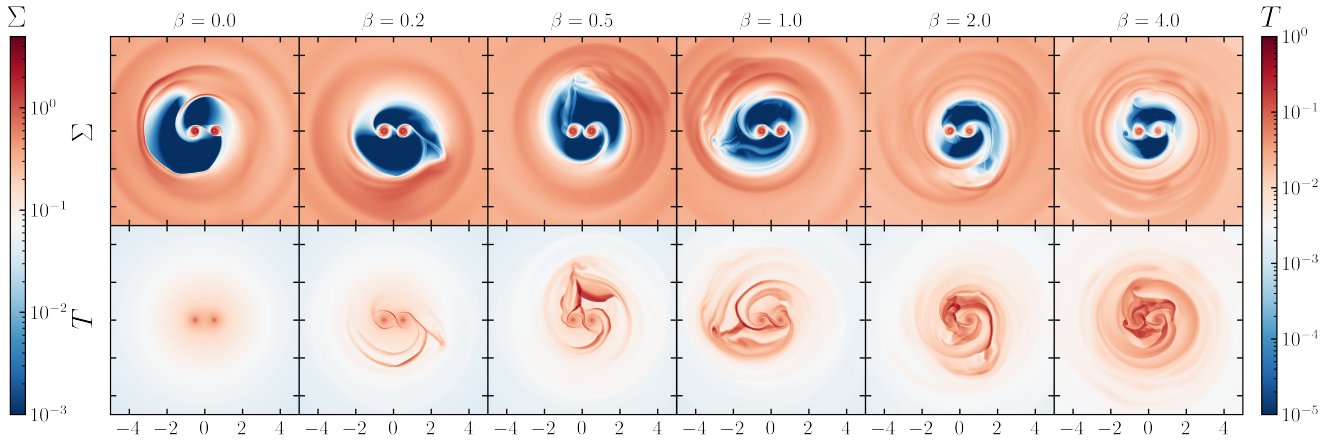


Figure A3. Similar to Figure 6, the density distribution (first row) and the temperature distribution (second row) in parameter survey subset *t1n3b-** with fixed α -viscosity.

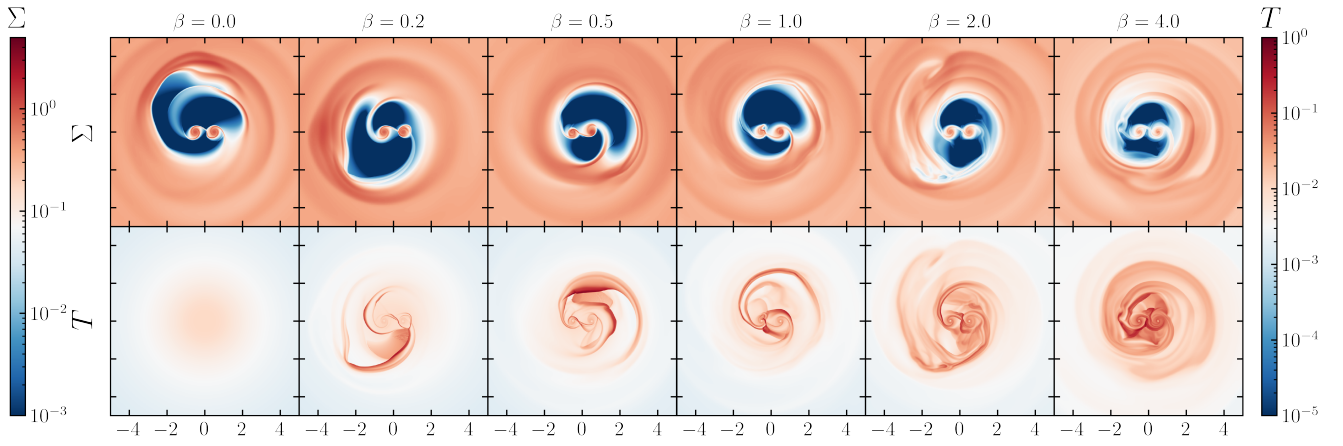


Figure A4. Similar to Figure 6, the density distribution (first row) and the temperature distribution (second row) in parameter study *t2n2b-** with fixed α -viscosity.

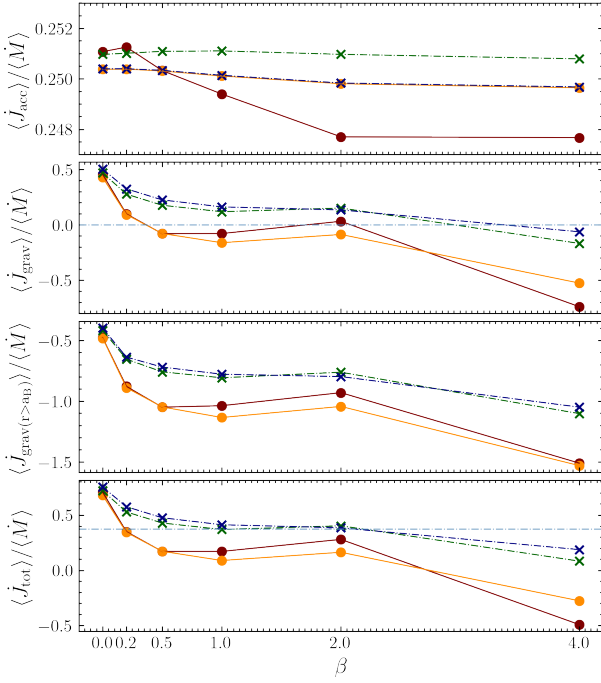


Figure A5. Similar to Figure 3, various specific torque components and the total specific torque of the CBD acting on the binary as a function of parameterized cooling time β in all subset employing a fixed viscosity profile. From the top to the bottom are (1) the specific accretion torque, (2) the specific gravitational torque, (3) the specific gravitational torque from the region $r > a_B$, and (4) the specific total torque. The horizontal dashed-dotted blue line in the second panel differentiates the sign of total gravitational torque, and the horizontal dashed-dotted line in the fourth panel illustrates the threshold of binary orbital evolution. The darkred, orange, darkgreen, and darkblue dots separately represent subset τ_{1n1b-} , τ_{2n1b-} , τ_{1n3b-*} , and τ_{2n2b-*} . The solid circles (solid lines) show the runs employing a constant viscosity; while the forks (dash-dotted lines) show the runs employing a fixed α -viscosity.

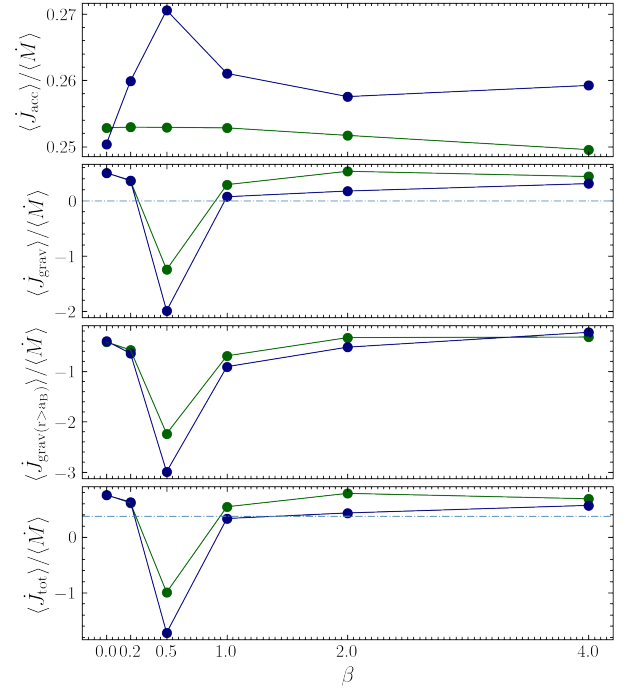


Figure A6. Similar to Figure A5, the darkgreen and darkblue dots separately represent subset τ_{1n3b-} and τ_{2n2b-} . A dynamically varying α -viscosity is adopted in these two subsets.